DEVELOPMENT OF HYDROGEN SEPARATION MEMBRANE IN
PALLADIUM BASED TERNARY SYSTEMS

A THESIS SUBMITTED TO
THE GRADUATE SCHOOL OF NATURAL AND APPLIED SCIENCES
OF
MIDDLE EAST TECHNICAL UNIVERSITY

BY

MEHMET MERT KÖSE

IN PARTIAL FULFILLMENT OF THE REQUIREMENTS
FOR
THE DEGREE OF MASTER OF SCIENCE
IN
METALLURGICAL AND MATERIALS ENGINEERING

January 2022

Approval of the thesis:

DEVELOPMENT OF HYDROGEN SEPARATION MEMBRANE IN PALLADIUM BASED TERNARY SYSTEMS

submitted by **MEHMET MERT KÖSE** in partial fulfillment of the requirements for the degree of **Master of Science in Metallurgical and Materials Engineering, Middle East Technical University** by,

Prof. Dr. Halil Kalıpçılar
Dean, Graduate School of **Natural and Applied Sciences**   _____

Prof. Dr. C. Hakan Gür
Head of the Department, **Metallurgical and Materials Eng.**   _____

Prof. Dr. Tayfur Öztürk
Supervisor, **Metallurgical and Materials Eng.**   _____

Examining Committee Members:

Prof. Dr. H. Emrah Ünalan
Metallurgical and Materials Eng, METU   _____

Prof. Dr. Tayfur Öztürk
Metallurgical and Materials Eng, METU   _____

Assoc. Prof. Dr. Hasan Akyıldız
Metallurgical and Materials Eng, KTÜN   _____

Assoc. Prof. Dr. Gülhan Çakmak
Metallurgical and Materials Eng., MSKÜ   _____

Assist. Prof. Dr. Fatih Pişkin
Metallurgical and Materials Eng., MSKÜ   _____

Date: 25.01.2022

I hereby declare that all information in this document has been obtained and presented in accordance with academic rules and ethical conduct. I also declare that, as required by these rules and conduct, I have fully cited and referenced all material and results that are not original to this work.

Name, Last name : Mehmet Mert Köse

Signature :

ABSTRACT

DEVELOPMENT OF HYDROGEN SEPARATION MEMBRANE IN PALLADIUM BASED TERNARY SYSTEMS

Köse, Mehmet Mert
Master of Science, Metallurgical and Materials Engineering
Supervisor: Prof. Dr. Tayfur Öztürk

January 2022, 88 pages

A study was carried out into dense metallic membranes for hydrogen separation. Two palladium-based system were characterized Pd-Mn-Ag and Pd-Co-Ni. Membranes were produced via sputter deposition in combinatorial geometry. For this purpose, sputter targets were arranged in triangular manner, and there were total of 21 substrates just above the targets. Membranes were screened via resistivity measurements under argon and hydrogen carried out up to 450 $^{\circ}$C. A reactivity index defined as resistivity under hydrogen over that in argon was used as an index of suitability of the thin film membranes for hydrogen separation.

The study has shown that Pd-Co-Ni system, except for small region close to Co corner, the rest of the ternary field had f.c.c. structure. Unfortunately, these membranes showed no reaction with hydrogen under 1bar of hydrogen pressure up to 450 $^{\circ}$C and therefore they were considered unsuitable as separation membranes. Pd-Mn-Ag ternary system was more fruitful. Similarly, the system had a wide compositional field with f.c.c. structure. These were on the side of Ag-Pd line and moreover, considerable fractions of these membranes were reacting with hydrogen implying that they may be suitable as separation membrane. Based on their reactivity

curve, and palladium content $Pd_{35}Mn_{13}Ag_{52,}$ $Pd_{56}Mn_{13}Ag_{31}$ and $Pd_{62}Mn_{18}Ag_{20}$ were selected as candidates for hydrogen separation.

Selected compositions were then sputter deposited on de-alloyed brass as support material for permeability measurements. Dealloying was carried out at 460 $^{\circ}$C for 4 hours under vacuum (10^{-6} mbar). This has yielded copper substrate with pores of approximately 1 μm in size. Thin film membranes of 5 μm thick were deposited on the nanoporous copper. Unfortunately, the measurements were not possible as the coated assembly were not argon tight. A thicker deposition 7 micron thick with substrate heating to 350°C also failed as these assembly was not structurally stable during testing.

ÖZ

PALADYUM ESASLI ÜÇLÜ SİSTEMLERDE HİDROJEN SAFLAŞTIRICI MEMBRAN GELİŞTİRME

Köse, Mehmet Mert
Yüksek Lisans, Metalurji ve Malzeme Mühendisliği
Tez Yöneticisi: Prof. Dr. Tayfur Öztürk

Ocak 2022, 88 sayfa

Bu çalışma, Pd esaslı üçlü alaşım sistemlerini esas almakta ve hidrojen ayrıcı membranlar için uygun alaşım kompozisyonlarının belirlenmesini hedeflemektedir. Çalışmada Pd-Mn-Ag ve Pd-Co-Ni olmak üzere iki sistem değerlendirilmiştir. Membranlar, kombinatoryal geometride sıçratma-çöktürme yöntemi ile üretilmiştir. Bu amaçla üçgen geometride yerleştirilen hedef metallerin hemen üzerinde toplam 21 adet altlık gene üçgen geometride yerleştirilmiştir. Bu tarzda oluşturulan membranlar direnç ölçümü ile 450 ^{o}C'ye kadar taranmış bu ölçümler hem argon hem de 1 bar hidrojen altında gerçekleştirilmiştir. Hidrojen altında hesaplanan özdirencin argondaki özdirence oranı reaktivite endeksi olarak tanımlanmıştır. İnce film membranın ayırıcı membran olabilme potansiyeli bu endeks temelinde değerlendirilmiştir.

Çalışmada, Pd-Co-Ni sisteminin Co köşesine yakın küçük bölge hariç geriye kalan bölgelerinde kompozisyonların y.m.k. yapıda olduğu tespit edilmiştir. Ne yazık ki, bu membranlar bu çalışmadaki koşullarda hidrojen ile reaksiyona girmemiş ve bu nedenle hidrojen ayrıcı membran olarak kullanılamayacakları değerlendirilmiştir. Pd-Mn-Ag sistemi Pd-Ag çizgisine yakın oldukça geniş bölgede y.m.k. yapı sergilemiştir. Direnç ölçümleri, geniş bir kompozisyon aralığında numunelerin dikkate değer hidrojen reaktivitesi sergilediğini göstermiştir. Bu numuneler

arasından reaktivite endeksi ve paladyum içeriği temelinde $Pd_{35}Mn_{13}Ag_{52}$, $Pd_{56}Mn_{13}Ag_{31}$ and $Pd_{62}Mn_{18}Ag_{20}$ hidrojen ayrıcı membranlar için aday kompozisyonlar olarak seçilmiştir.

Seçilen kompozisyonlar daha sonra geçirgenlik testine tabii tutulmak üzere alaşımsızlaştırılmış pirinç üzerine kaplanmıştır. Bu amaçla pirinç 460 ^{o}C'de 4 saat vakum altında (10^{-6} mbar) alaşımsızlaştırılmıştır. Bu işlem sonucunda, yaklaşık 1 µm boyutunda gözeneklere sahip bakır altlık elde edilmiştir. Nano-gözenekli bakır üzerine 5 µm mikron kalınlığında kaplanan membranlar argonla yapılan gaz sızdırmazlık testinden geçememiştir. Takiben 350 ^{o}C'de ısıtma yapılarak 7 µm kalınlığında membranlar kaplanmış ancak yapısal bozulma nedeni ile bu membranlardan da güvenilir sonuç alınması mümkün olamamıştır.

Anahtar Kelimeler: Hidrojen Ayrıştırma, Yoğun Metalik Membranlar, Paladyum Esaslı Alaşımlar, Pd-Mn-Ag, Pd-Co-Ni, Alaşımsızlaştırma

To my friends,

and my family…

ACKNOWLEDGMENTS

First, I would like to express my gratitude to Prof. Dr. Tayfur Öztürk. His virtuosity, guidance, vision, support, and kindness taught me a lot. It made me improve myself in a way I could only imagine a few years ago. It was a pleasure and a privilege for me to work with him.

I would like to thank Dr. Fatih Pişkin for his assistance and patience throughout the study. This work became so much easier with his help and his experience.

Without my friends' assistance, friendship, and support, this work would not be possible for me to fulfill. I would like to thank to M. D. Ali Doğan, Fahrettin Kılıç, İshak Emre Ömür, Burak Can Şahin, and Ekin Yıldızhan.

I am also grateful to all the staff of the Metallurgical and Materials Engineering Dept. and I would like to thank to my laboratory fellow: Fahrettin Kılıç, Havva Eda Aysal, Yiğit Akbaş, Hilal Aybike Can, Necdet Özgür Darıcıoğlu, Ramin Babazadeh, Necmi Avcı and Eren Şimşek for their efforts, patience, and readiness to help. I also want to thank Gökhan Polat for his assistance and patience during experimental studies.

Expressing my gratitude to my beloved family is impossible to put into words. Contributions that they made are not only to my thesis work but also my whole life perception. Especially for the moral support during the hard times that I had been through, I am grateful to Gülcan Atalay, Ali Necip Köse, Dr. Özge Köse, and Zeynep Köse Kaunas. My thesis would not be completed without their presence that makes me feel confident.

TABLE OF CONTENTS

LIST OF TABLES

LIST OF FIGURES

xiv

CHAPTER 1

INTRODUCTION

Hydrogen is considered to be an energy carrier to reduce greenhouse gas emissions. The use of hydrogen yields only water vapor; therefore, it gives no harm to the environment since no CO_2 emission to the atmosphere takes place during the consumption.

Hydrogen is produced in a variety of ways such as electrolysis, steam reforming of methane (SRM), gasification of biomass, etc. Today, SRM and biomass gasification dominate the world's hydrogen production[1]. 'Syngas' produced in this way contains a mixture of gases, mainly CO, CO_2, in addition to H_2. An additional separation step is required to obtain pure hydrogen. Also, it should be mentioned that hydrogen produced from renewable energy, i.e., solar and wind energy, may be injected into the natural gas grid as a practical storage method. Therefore, a separation membrane may be needed so as to separate hydrogen from methane in the gas grid.

Hydrogen purification can be carried out by several methods such as cryogenic distillation, Pressure swing adsorption, or purification by separation membranes. Pressure swing adsorption is a very common technique that is based on adsorbing impurity gases in zeolites by applying positive pressure[2]. 99.999% hydrogen can be obtained as a result of this purification method. However, PSA is not practically applicable for small-scale systems[3]. In addition, the cost of purification is quite high.

Separation membranes offer a suitable solution to the purification of hydrogen. They can be integrated into a variety of systems quite easily. Separation membranes may

be divided into two categories: porous separation membranes and dense metallic membranes. In porous separation membranes, purification depends on gases' mean free path and pore sizes. Basically, four mechanism lies behind the separation in the porous membranes. These are Knudsen diffusion, Surface diffusion, Capillary diffusion, and Molecular sieving[4].

The separation principle in dense metallic membranes is different and more appealing than that of porous separation membranes. Separation basically takes place by the solution of hydrogen in the membrane and diffusion of atomic hydrogen through its thickness. Since only the hydrogen is dissolved in the membrane, 100% purity is achieved.

Pd has remarkable hydrogen solubility and diffusivity compared to most other metals. However, the Pd-H phase diagram shows that phase transformation is present at 293°C, which causes α phase to transform β-hydride. This phase transformation causes lattice expansion, and as a result, Pd may be embrittled. Alternatives for Pd fall into three distinct groups, namely f.c.c., b.c.c., and amorphous metallic membranes.

Amorphous membranes have an open structure which is advantageous in terms of solubility and diffusivity of hydrogen. Generally, they combine elements such as Zr, Ni, Cu, and Al, and their alloys[5]. Although excellent permeabilities have been achieved, amorphous metallic membranes may crystallize after being exposed to high operating temperatures, which adversely affect their permeability.

b.c.c. membranes exhibit better permeability than Pd since atomic packing is lower in b.c.c. than that of f.c.c Pd. However, high hydrogen solubility causes excessive lattice distortion. Therefore, hydrogen embrittlement is a common problem in b.c.c membranes. Also, these membranes require an additional process of catalytically activating their surfaces. Thus, Pd-alloy coating may be necessary.[6]. Although their ability to adsorb hydrogen is high, they have limited applicability.

Currently, dense metallic membranes have f.c.c. lattice structure. These membranes exhibit greater mechanical and chemical stability. Despite relatively low permeability compared to other metallic membranes, they are commonly used for separation purposes in many applications. Pd-23at.%Ag is the most popular as it suppresses the phase transformation, yielding a durable membrane[3].

The main problem in Pd-23at.%Ag is its high cost. Currently, efforts are concentrated on reducing its cost as well as improving its permeability. One approach for this is to decrease membrane thickness. Using thin film membrane can reduce the cost and would improve the flux across the membrane. An alternative approach is to alloy Pd with other less costly elements.

The current study aims to produce Pd-based thin film membranes. Pd-Co-Ni and Pd-Mn-Ag ternary alloys with 3 μm thickness have been produced by magnetron sputtering in combinatorial geometry and examined for their hydrogen solubility via resistivity measurement. Having selected candidate compositions by considering their phase structure and hydrogen reactivity, membranes are reproduced with the same method for permeability testing.

Following a general introduction, the thesis comprises a total of 6 chapters. A brief review of dense metallic membranes is given in Chapter 2. This is followed by experimental techniques used in the present work, which comprises combinatorial deposition of thin films methods used resistivity and permeability measurements. Pd-Co-Ni and Pd-Mn-Ag ternary systems are evaluated in Chapter 4 and Chapter 5, respectively, in terms of film structure and their resistivity to identify candidate compositions as separation membranes. The dissertation is finalized in Chapter 6, where the general conclusions and recommendations are given.

CHAPTER 2

HYDROGEN PURIFICATION BY MEMBRANES

2.1   Introduction

Hydrogen can be produced in a variety of ways. Apart from electrolysis which produces pure hydrogen, the other methods involve a mixture of gases. Most notable sources of hydrogen make use of syngas generated from coal or natural gas. Generation of syngas from natural gas generally takes place in two steps; Reforming of methane (850 ^{o}C) and water gas shift reaction where the temperature involved are 350-200 ^{o}C [7]. At the end of the process gas mixture can typically contain 75 vol.% of hydrogen[8].

Another source of hydrogen is biomass gasification. Biomass gasification is a process that is combustion of solid fuels such as agricultural wastes, food wastes, wood, and paper wastes. Generally, the process takes place at elevated temperatures above 600 ^{o}C and product gas comprises CO, CH_4, CO_2 and H_2. Percentage of the gases are typically 35-40 vol.% for H_2, 20-25 vol.% for CO_2, 22-25 vol.% for CO, 9-11 vol.% for CH_4 and <1 vol.% for N_2[9].

Recently, a new practice has been to generate hydrogen from renewable sources, i.e., solar or wind energy via electrolysis and store them in the gas pipelines. This also represents a new environment where hydrogen is mixed with a mixture where a greater portion is methane. According to the recent two projects GRHYD[10] and HyDeploy[11] hydrogen injection through natural gas pipelines is safe up to 20 vol.%. Therefore, hydrogen extraction from the gas pipelines may be desired for use in fuel cells and similar. This application requires membranes that will operate at significantly lower temperatures.

2.2 Separation Mechanism

High purity hydrogen can be obtained from several different techniques such as pressure swing adsorption, cryogenic distillation, or hydrogen selective membranes.

Cryogenic distillation methods is similar to any distillation method[12]. The operation takes place under -195 °C, and gases apart from hydrogen can be condensed to liquid form. As a result, hydrogen remains in the gas phase since its boiling point is -252 °C[13]. However, this method has some limitations. Only 99% hydrogen purity can be obtained, and since the system requires complicated cooling equipment, the process is expensive to operate and can only be used in stationary systems[14].

Pressure swing adsorption is based on adsorbing impurity gases on porous media by applying positive pressure and desorption from the same media by reverse process[2]. Generally, zeolites are used as porous media and up to %99.999 hydrogen purity can be achieved[2]. The cost of production is quite high due to high compression involved. This is a large scale industrial system not easily adaptable to small scale applications[3].

Hydrogen selective membranes may be either porous or non-porous. Porous membranes are suitable for gas mixtures involving molecules of different sizes. There are four mechanisms involved in porous membranes; surface diffusion, Knudsen diffusion, capillary condensation, and molecular sieving, Figure 2.1[4].

(a)　　　(b)　　　(c)　　　(d)
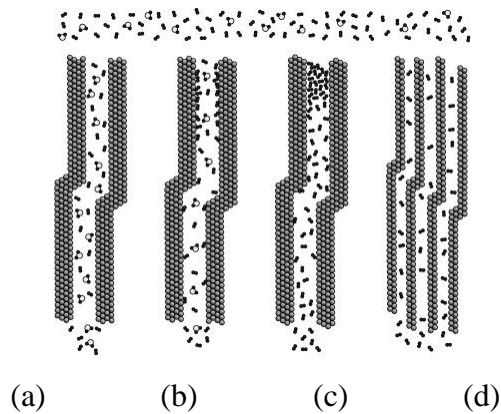
Figure 2.1 Schematic view of (a) Knudsen diffusion, (b) surface diffusion, (c) capillary condensation, (d) molecular sieving [4].

In the Knudsen diffusion, mean free paths of the gasses play a key role in separation. In gas mixtures, gases with different molecular weights can be separated by means of their mean free paths. Surface diffusion is another diffusion mechanism in porous membranes. Elementally, purification occurs by the diffusion of atoms from the pore walls. However, surface diffusion is not a viable mechanism because pore walls in use could be blocked in time and may reduce their effectiveness with time. Capillary condensation occurs when permeating gas condensates along with the pores, and only the same gases can be solved in the condensed phase. This mechanism provides good selectivity depending on the gas composition.

The most common mechanism in hydrogen separation by porous membranes is molecular sieving. In this mechanism, pore sizes should be not greater than 1 nm in size in order to select small gas molecules. Alumina and silica[15] are the commonly used porous membranes. However, none of these porous membranes provides good purity levels with respect to dense metallic membranes.

2.3　　Hydrogen Separation by Dense Metallic Membranes

Dense membranes operate on the solution-diffusion mechanism. Separation in these membranes occurs first by the dissociation of H_2 molecules on the surface of the

7

membrane into H atoms. Then interstitial dissolution of H atoms takes place in the body of the membrane. Hydrogen then diffuses across the membrane due to concentration difference as a result of pressure difference at the feed and permeate side. Hydrogen atoms, upon reaching the permeate side, recombine to hydrogen molecule, which then desorbs from the surface, Figure 2.2.

There are different types of dense metallic membranes such as amorphous, b.c.c. and f.c.c. structured membranes, yet the separation mechanism is all the same for these three types, as explained above.
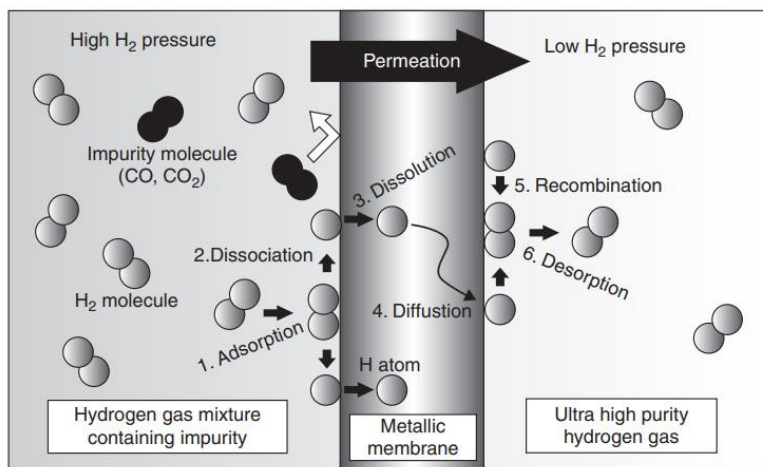
Figure 2.2 Hydrogen separation through dense metallic membranes[16]

Diffusion of hydrogen in metals can be explained by Fick's first law;

$$J = -D \frac{\partial C}{\partial x}$$

Eqn.2.4

Where J is the flux and D is the diffusion coefficient and $\partial C/\partial x$ is concentration gradient of hydrogen. Difference in the hydrogen concentrations at the entry and the exit side of the membrane drives the process.

According to the Sievert's law, hydrogen dissolution into metals is a function of square root of pressure, i.e.;

$$S = \frac{C_{H2}}{P_{H2}^{1/2}}$$ *Eqn. 2.5*

Integration of Sievert's law into Fick's First law by $\partial P/\partial x$ derivation gives;

$$J = DS \frac{\partial P_{H2}^{1/2}}{\partial x}$$ *Eqn.2.6*

Which can be re-written for the membrane as a whole ;

$$J = DS \frac{\Delta P_{H2}^{1/2}}{x}$$ *Eqn. 2.7*

Here, ΔP_{H2} refers to hydrogen pressure difference eat the entry and exit side of the membrane and x is membranes' thickness. The term in Eqn.2.7, D*S is the product of diffusivity and solubility. This is expressed as permeability, i.e.

$$k = D.S$$ *Eqn. 2.8*

The unit of flux is mole/m^2.s,i.e. number of moles transported through the membrane across a unit area per unit time. This quantity is not a materials property as it depends on the thickness as well as on the concentration gradient. Permeability, i.e. on the other hand, is a material property which has a unit of mol/m.s.Pa$^{1/2}$.

Thus, flux in terms of permeability may be written as

$$J = \frac{k}{x} (P_{Inlet}^n - P_{Outlet}^n)$$ *Eqn. 2.9*

n is the gas constant, in Sieverts law, Eqn. 2.5 mostly taken as 0.5.

Permeability is temperature dependent and obeys Arrhenius equation.

$$k = k_0 \, exp\left(\frac{-E_k}{RT}\right)$$

Dense metallic membranes are divided into three groups in terms of their structure namely, face centered cubic, body centered cubic and amorphous membranes.

2.3.1 Amorphous Metallic Membranes

Amorphous metals have relatively more open structure which would enhance the solubility of hydrogen[17]. Generally, elements such as Zr, Ni, Cu, and Al are used in the production of amorphous membranes. Operations temperatures are set below their glass transition temperatures as extended use close to transition temperature leads to the formation of crystalline regions in the alloy [17].

To see the crystallization effect on permeability, Itoh et al. [18] used Pd-Si binary alloy in both amorphous and crystalline forms. They prepared different compositions of amorphous Pd-Si ribbons with 5 mm diameter and 40 μm thickness by rapid quenching. Crystallization is provided with heat treatment which is fulfilled above their crystallization temperature. They concluded that $Pd_{0.825}Si_{0.175}$ alloy in amorphous form exhibits five times higher permeability than the crystalline form of the same composition. They further stated that no hydrogen embrittlement is seen for amorphous alloy, unlike its crystalline form.

Common method for using amorphous membranes is to apply Pd coating onto the membrane surface. Lai et al. [17] examined the hydrogen permeability of both Pd-coated and non-Pd coated membranes. They produced amorphous $Cu_{63}Zr_{37,}$ $Cu_{46}Zr_{54,}$ and $Cu_{40}Zr_{60}$ alloys by splat quenching. The thicknesses of the membranes were 45 micrometers, and their diameters were 20 mm. After successful production, Pd coating was achieved on the surface by DC sputtering. They concluded that the higher permeabilities could be reached with the Pd coating process.

Similarly, Hara et al. [19] produced Zr-Ni amorphous membranes by arc melting. They concluded that $Zr_{36}Ni_{64}$ amorphous binary alloy exhibit hydrogen permeability of around $9x10^{-9}$ mol/m.s.Pa$^{1/2}$ at 350°C. In a separate study, Hara et al. [20] produced $Zr_{36}Ni_{64}$ ribbons by quenching using copper rollers. After producing 40 micrometer thick ribbons, they coated both sides of the membrane with Pd with the thickness of 100 nm. As a result, they reached a similar permeability value with the pure palladium, namely $k=5x10^{-9}$ mol/m.s.Pa$^{1/2}$ at 350 °C.

Yamauara et al. [21] fabricated $(Ni_{0:6}Nb_{0:4})_{45}Zr_{50}X_5$ alloy where X = Al, Co, Pd or P. Membranes were fabricated in 20 mm diameter and 50 μm thick. They then coated the membranes with Pd on both sides by sputtering or electroless plating method. For every X element, Pd coating with sputtering technique gives better permeability compared to electroless plating. They report permeability values of $2.46x10^{-8}$ mol/m.s.Pa$^{1/2}$ and $2.34x10^{-8}$ mol/m.s.Pa$^{1/2}$ for $(Ni_{0:6}Nb_{0:4})_{45}Zr_{50}Co_5$ and $(Ni_{0:6}Nb_{0:4})_{45}Zr_{50}Cu_5$ alloy, respectively. The permeability values reported are almost 2.5 times that of pure palladium.

Regarding these studies, despite their low cost and resistance to hydrogen embrittlement and quite high permeability, the amorphous membranes are difficult to produce and have not yet found applications in practice.

2.3.2   b.c.c. Dense Metallic Membranes

b.c.c. metals have atomic packing factor of 0.68 and therefore have relatively open structure. Therefore, it can have high solubility for hydrogen. The lattice incorporates 3 octahedral and 6 tetrahedral sites[22]. Hydrogen atom movement takes place by leaping between octahedral and tetrahedral sites. Examples of b.c.c. membranes are given in Table 2.1[6]. The permeability of palladium silver alloy ($Pd_{77}Ag_{23}$ in at.%), a commercial f.c.c. composition is also included in this table. It is seen that b.c.c. membranes have permeability values higher than that of $Pd_{77}Ag_{23}$.

Table 2.1 Permeabilities of some b.c.c. membranes at 400 $^\circ$C[6]. Commercial Pd-Ag alloy is also included which is an f.c.c. alloy [23].

Metals/Alloys	Permeabilities (mol/m.s.Pa$^{0.5}$)
$Pd_{77}Ag_{23}$	2.6×10^{-8}
V	3×10^{-7}
Ta	2×10^{-7}
Nb	3×10^{-6}
$V_{85}Ni_{15}$	3×10^{-8}
$V_{90}Pd_{10}$	3.86×10^{-8}
V-10Al	1×10^{-7}
$V_{89}Ni_6Co_5$	5.3×10^{-8}

Open lattice structure in b.c.c. also favors high diffusivity. Unfortunately, excessive hydrogen solubility results in hydrogen embrittlement[6].

Embrittlement can be overcome by alloying the membranes with specific transition elements. Commonly used alloying elements are Co, Cr, and Al [24]. Besides, Zr, Mo, and Ru elements are also considered to be good alloying elements because these elements result in an increase in hydride formation enthalpies and therefore avoid hydrogen embrittlement caused by stable hydrides[25].

Komiya et al [25] studied a number of Nb-M alloys where M is for Zr, Ru, Mo, Rh, and Pd. They produced the alloys by arc melting, and pressure-composition-temperature measurements were carried out. They observed that alloying in small amounts yields significant differences in hydride phase formation. They found that 3-5 % Mo or Ru addition to Nb destabilizes hydride phases, namely β (NbH) and δ (NbH2); therefore, hydrogen embrittlement could be avoided.

Hashi et al[26] produced Nb-Ti-Ni alloys as membranes by arc melting. The structure was mainly eutectic, composed of a Nb-Ti solid solution and TiNi intermetallic. Hydrogen permeation took place in a solid solution. However, they

found that two-phase structure makes the membrane more durable for hydrogen embrittlement. Also, the volume expansion was less. For instance, single-phase alloy, Nb83Ti13Ni4 exhibits brittle behavior under hydrogenation while two-phase alloy Nb39Ti31Ni30 consisting of eutectic and primary phase remained robust. Also, the permeability of this composition reached up to 2x10-8 molH2.m-1.s-1.Pa-0.5, at 400 oC, which is nearly the same as that of Pd77Ag23 alloy.

As it has been the case for amorphous membranes, Pd coatings are often applied onto b.c.c. membranes which not only prevents the oxide formation but also provides catalytically activation of surfaces. Many studies [23,27–30] show that the Pd coating below 1 μm thickness helps inhibiting oxide formation and by means of this, permeability values reach higher levels. For instance Cooney et al. [31] studied V, Ta, and Nb membranes coated with Pd. This was achieved via DC sputtering, and 100 nm Pd coating was obtained on the surface of the membranes. They achieved in Nb membrane permeability value of $3x10^{-7}$ mol/m.s.Pa$^{0.5}$ at 500 ^{o}C (the permeability of Pd$_{77}$Ag$_{23}$ commercial alloy was $2.69x10^{-8}$ mol/m.s.Pa$^{0.5}$). According to this study, Pd did not dissolve in the body of the membrane and as a result the delamination occurred on the surface and the flux was reduced as a result.

b.c.c. membranes are an important group among hydrogen selective membranes as they have quite high permeability values. Solutions could be provided for hydrogen embrittlement, and it is also possible to prevent surface oxidations. Unfortunately, these membranes have generally limited formability, and therefore, the processing into thin sheets or tubes is a challenging task.

2.3.3   f.c.c. Dense Metallic Membranes

Pd is the most common f.c.c. metal used as hydrogen separation membranes. As stated by Thomas Graham[32], Pd has the ability to absorb hydrogen 600 times more than its own volume without any shape distortion. This is attributed to Pd's high affinity for electrons due to its overlapping energy band between 4d and 5s energy

bands. This facilitates hydrogen-palladium interaction on the surface and enables hydrogen molecule to dissolve in the body of the metal as atoms.

Also, having f.c.c. structure provides Pd resistance to hydrogen embrittlement. With respect to b.c.c. metals, Pd can dissolve less hydrogen due to dense packing of the lattice. Therefore, this metal is less susceptible to hydrogen embrittlement.
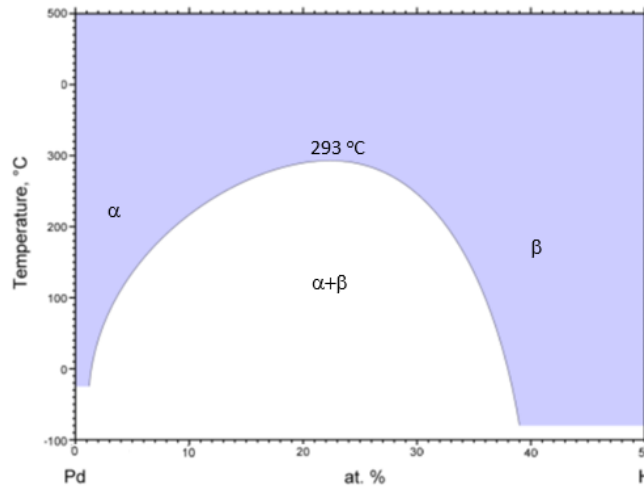
Figure 2.3. Pd-H phase diagram[33]

Figure 2.3 shows binary phase diagram of Pd-H[33]. As can be seen, the diagram incorporates two phases: a solid solution (α) and a hydride phase (β). Above 293 ºC, only the α phase exists. Below 293 ºC α and β are present together. Both phases are cubic with lattice parameters of 3.889 Å and 4.025 Å for α and β, respectively. Therefore, upon cooling from high temperature $\alpha \rightarrow \alpha + \beta$ transformation takes place leading to typically 10% volume change. This volume change results in the distortion of the metal. To overcome this, Pd can be used above 293 ºC, avoiding the exposure of the alloy to hydrogen at a lower temperature [3].

Alloying elements can reduce $\alpha \rightarrow \alpha + \beta$ transition temperature. Therefore, α phase may be stable over an extended temperature range. For this purpose, silver[34], gold[35], platinum[36] and yttrium [37] are used as alloying elements. Table 2.2 lists some of these alloys and their permeabilities at 350 ºC.

14

Table 2.2. Permeability of Pd and Pd-based alloys

Alloy (%at.)	Permeability x10^8 (mol/m.s.Pa$^{0.5}$)	References
Pure Pd	1.20	[38]
Pd$_{77}$Ag$_{23}$	3.21	[39]
Pd$_{92}$Y$_8$	3.82	[37]
Pd$_{95}$Au$_5$	1.49	[35]

The best hydrogen permeabilities have been achieved using Pd-Y alloys with a permeability equaling 3.82×10^{-8} mol/m.s.Pa$^{0.5}$. However, using Pd$_{92}$Y$_8$ alloy in practice is harder in terms of fabrication. Due to high work hardening rate, the mechanical processing of Pd-Y alloy is quite challenging[37].

Flanagan et al[35] found that alloying palladium with %5 gold yields higher permeability as compared to pure palladium. Also, with Au H$_2$S and CO poisoning effect is reduced quite significantly[35]. The problem with gold is its high cost.

Commercially, Silver is the most notable alloying element used for Pd-based membranes. The alloy Pd$_{77}$Ag$_{23}$ is commonly accepted as a hydrogen separation membrane with a permeability value of 3.21×10^{-8} mol/m^2.s.Pa at 350 $^{\circ}$C[39]. Alloying Pd with silver not only result with higher permeability, but also the reduction in transition temperature is quite pronounced [40]. Under 2 MPa hydrogen pressure α to β transition which occurs at 293 $^{\circ}$C in pure palladium decreases below room temperature with Ag addition [41]

It should be mentioned that Pd-Ag membranes may be adversely affected by gas mixtures containing H$_2$S and CO, which might lead to the formation of carbides and sulfides. These contaminants on the surface retards the permeation of hydrogen.

Zhang et al. [42] has used electroless plating technique to produce Pd-Ni membrane for hydrogen separation. The membrane was several micrometers thick plated onto porous alumina tube substrates with the pore size 0.3 μm and the porosity of 40%.

While conducting permeability tests, they first used argon gas for leakage control and then applied the same procedure with hydrogen. Hydrogen is given from the outside of the tube and collected from the inside. Permeated gases flow rates are measured with a bubble flowmeter. They concluded that $Pd_{95}Ni_5$ composition had a noticeable permeability for hydrogen with a value of $3.1x10^{-6}$ mol/m^2.s.Pa at 400 ^{o}C.

Piskin et al. [43–45] have studied different Pd binary and ternary alloys using magnetron sputtering. The aim of these studies is to find alternative compositions to commercial hydrogen separation membrane $Pd_{77}Ag_{23}$ alloy. For this purpose, they examined the Pd-Ag-Ni, Pd-Ag-Ti, Pd-Nb-Ti ternary alloy compositions. They produced 21 different compositions for each ternary system. They screened these alloys via electrical resistivity measurements taken under argon and hydrogen atmosphere. Selected compositions are melted, cast, and rolled to 100 μm thick foil for permeability measurements. Although the permeability values were not higher than that of the commercial alloy $Pd_{77}Ag_{23}$, they report composition which contains 20 at.% less Pd.

2.4   Support for Dense Metallic Membranes

When separation membranes are quite thick, say 50 microns or more, various substrates can be used to support the membrane. These would be porous ceramics or, preferably, porous metals produced via powder metallurgy. However, when the membranes were produced via electroless deposition or via PVD methods, the membranes were quite thin, typically 10 microns or less. In such cases, there are stringent requirements for substrates.

According to Mardilovich[46], membranes to be deposited as thin films requires thickness to be three times that of the biggest pore in the substrate. This 3-to-1 rule requires that for membranes, for instance, 3-5 μm thick substrates need to be nanoporous, i.e., pore sizes should be 1 micron or less.

There are a number of methods that can be used for the fabrication of support materials for separation membranes. These include the use of nanoporous ceramics and glasses, nanoporous metals produced via either thermal[47] or electrochemical dealloying[48], or a method based on selective dissolution of a co-polymer[49]. Here we will briefly review the substrate preparation involving nanoporous ceramics and glasses as well as vacuum thermal dealloying.

Ceramic and glass substrates used as a support material include alumina[50], YSZ[51], silica glass [52] Vycor glass[53] and stainless steel[54].

Porous stainless steel (PSS) produced via powder metallurgy may be modified with fine ceramic powders so as make it suitable as support material. Zahedi et al. [55] used porous stainless steel with initial average pore sizes of 10 μm and electrodeposited WO_3 onto it so as to reduce the pore sizes down to several nanometers. Following the pore size modification, they coated 12 μm thick Pd via electroless deposition and obtained a permeability value of 2.06×10^{-8} mol/m.s.$Pa^{-0.5}$. As a result, a selectivity value (J_{H2}/J_{N2}) of approximately 14,000 had been reached.

Microporous alpha alumina was used by Ilias et al. [56] with nominal pore sizes of 150 nm as a substrates of Pd coating. They produced two Pd film thicknesses of 8.5 μm and 12 μm via electroless deposition and achieved permeabilities of 1.46×10^{-8} mol/m.s.$Pa^{-0.7}$ and 3.87×10^{-8} mol/m.s.$Pa^{-0.5}$ at 300 °C, respectively. They tested the membrane with argon and reported that permeate side of the system did not contain any argon therefore, the membranes are fully selective.

Lewis et al. [36] studied electroless deposition of Pure Pd and Pd-Pt alloys onto YSZ porous supports with a maximum pore size of 2 μm. The thicknesses of the membranes varied between 4 to 12 μm. They achieved in Pd-26%Pt a good permeability with 2.92×10^{-9} mole/m^2.s.$Pa^{0.5}$ and selectivity was 13,393 (J_{H2}/J_{N2}).

Altinisik et al. [52] used porous silica glass with average pore sizes of 1 μm. They coated Pd layer of 15 μm thick onto the porous glass via electroless deposition. They reported that at 200 °C, the   hydrogen permeance rate of the membrane was 0.5

$cm^3/cm^2.s$. Hydrogen selectivity tested with nitrogen was 7 (J_{H2}/J_{N2}), which is quite low. In a similar study, Yeung et al. [53] studied the Pd-Vycor glass composite membrane fabrication by electroless plating. They confirmed the suitability of vycor glass for Pd coating by deposition. In this study, 0.9 μm thick Pd was deposited onto porous vycor glass tube with 5 nm surface pore size.

Jayaraman et al. [57] have used RF sputtering to deposit Pd thin films of less than 1 μm thick.. They used α and γ alumina mesoporous substrates with approximately 150 nm pore sizes. The gas tightness of these membranes is measured by nitrogen, and as a result, they reported that the surface was dense and smooth. In a similar study by Jayaraman [58] sputter deposited Pd-Ag alloy thin films 250-500 nm thick over alumina substrates with 3 nm pore size. However, pinholes formed in the coating which reduced the hydrogen selectivity. Gobina et al. [59], have used vycor glass as substrates and deposited Pd-Ag film via sputter deposition. Vycor glass had average 4 nm pore sizes. Film thicknesses were between 5 to 8 μm, and they concluded that membranes are entirely hydrogen selective with a permeability value of 2.16 x 10^{-5} cm^3-$cm/cm^2.s.atm^{0.5}$.

Vacuum Thermal Dealloying Vacuum Thermal dealloying makes use of single-phase or two-phase alloys and involves removal of one of the elements via annealing under vacuum. The elements removed are Zn, Mg, or similar for the reason that they have high vapor pressure; Zn has a vapor pressure of 1 Torr at 487 ^oC [60]and that of Mg is 7 torr [61]. These elements, when combined with Ni, Co or Cu could be successfully dealloyed as the evaporation rates of the elements are quite different. For example, for Cu-Zn, the vapor pressure ratio,i.e. pZn/pCu is approximately 2.14 $\times 10^{13}$ at 500 °C[62].

Sun et al.[62] used $Cu_{30}Zn_{70}$ brass made up of γ+ε phases. Samples were dealloyed in vacuum at 10 Pa at 450, 500, 550 and 600 ^oC for 3 hours. They formed three-dimensional continuous porous structure with 2 μm pore size. They found that as the temperature of dealloying was increased above 600 ^oC, porous structure was lost as

a result of sintering. The optimum temperature for physical dealloying was reported to be 500 °C.

In a similar study by Ren et. al. [63], dealloying of three alloys; $Cu_{50}Zn_{50}(\beta)$, $Cu_{40}Zn_{60}$ (γ), and $Cu_{30}Zn_{70}$ ($\gamma+\varepsilon$) were examined. Pore sizes varied between 1 to 5 μm. Diameters of pores increased with increasing Zn content for the same thermal dealloying conditions. Smallest pore size was 1±1 micron obtained for $Cu_{50}Zn_{50}$ when dealloyed 500 °C for 3 hours.

Ni-Zn, Ge-Zn, Co-Zn alloys were also examined for dealloying [47,63,64]. In the case of Ni-Zn, the temperature of dealloying was 550-700 °C and those for Ge-Zn was 350-500 °C. As a result, nanoporous nickel or germanium with connected ligament structure were obtained where the smallest pore sizes were 0.4 and 0.75 μm respectively.

Kosmidou et al[65], alloyed Nb, Ta, V, Mb elements with magnesium using magnetron sputtering. They produced 0.25 μm films. The films were then exposed vacuum for thermal dealloying. For this purpose, the chamber was taken under vacuum, heated to 600 °C for 2 hours using quartz lamp. They obtained a ligament size of 19 nm but did not report the pore size.

CHAPTER 3

MATERIALS AND METHODS

3.1 Combinatorial Deposition of Thin Film Membranes

Thin film alloys were produced via sputter deposition. The vacuum chamber was 500x500x500mm, Figure 3.1. It incorporates four sputter guns, though, in the present work, only three guns were used. They were placed at 120° intervals on a circle 350 mm in diameter. Stem to stem distance between the target holders was 300 mm.
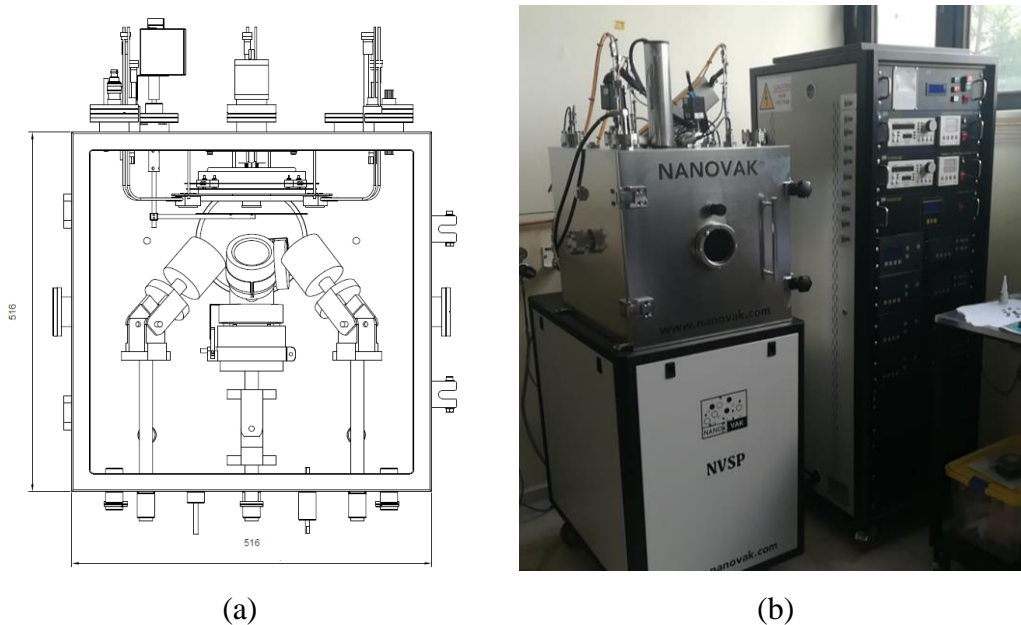
Figure 3.1. (a) Schematic representation of magnetron sputtering chamber, (b) photograph of magnetron sputter setup.

Targets were aligned with respect to the central target. For this purpose, the central target was aligned vertically, as shown in Figure 3.2(a). In this position, the distance of the central sputtering gun to the substrate plane is 92.5 mm. (Substrate plane housed three sensors for thickness monitoring. These sensors were placed on a circle of 180 mm, each located just above the respective guns). Subsequently, the other

sputtering guns were adjusted. Here, each peripheral sputtering gun was tilted so that the lower end of the target housing was in the same plane as the central gun, Figure 3.2(b). This positioning fixes the tilting angle of the sputter guns. Rotational positionings of the guns were made by adjusting and fixing in such a way that the measurement of two thickness monitors away from the gun did similar readings.

(a)   (b)
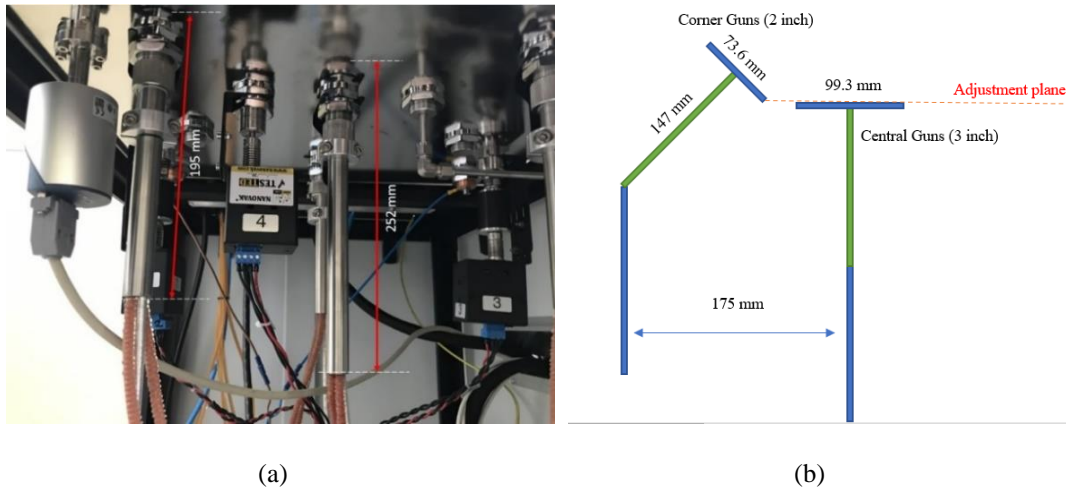
Figure 3.2. (a) Positions of the sputtering guns outside the chamber. Adjusted as to central sputtering gun $Z_{\text{stem-out}}$= 252 mm other sputtering guns $Z_{\text{stem-out}}$ = 195 mm (b) other sputtering guns position adjustment by looking at central sputtering gun.

Substrate magazine was placed in the substrate plane above the sputter targets, which had a diameter of 150 mm. The magazine incorporates a total of 21 substrate holder, each 19 mm diameter. The substrates had a triangular distribution mimicking the targets underneath, Figure 3.3. Triangular area had an equilateral shape with edges of 130 mm.

(a)   (b)
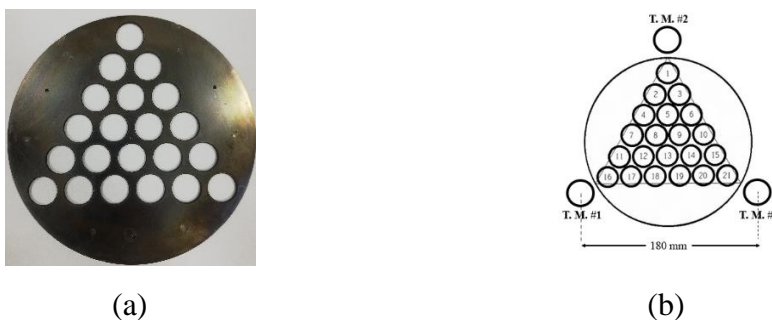
Figure 3.3. (a) Photograph of substrate magazine. (b) the positions of sensors for thickness monitors. (c) image of the vacuum chamber while in operation.
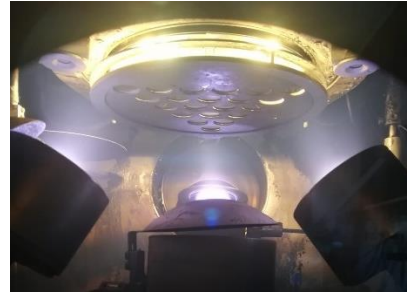
(c)

Prior to every deposition process, the vacuum chamber was thoroughly cleaned using ethanol. Substrates before loading onto substrate magazine were thoroughly cleaned. For this purpose, substrates were cleaned first by distilled water in an ultrasonic bath for 15 minutes, then rinsed with ethanol and acetone. Then, substrate magazine is positioned above the guns, and the chamber is evacuated to the base pressure level 10^{-7} mbar. While under vacuum, the chamber was heated to 300 $^{\circ}$C with quartz lamps so as help reduce moisture in the vacuum chamber.

After reaching desired base pressure, argon switched on, activating the respective flow controller with 10 scc/min flux. For plasma ignition, adjusting the gate valve connected to turbomolecular pump argon pressure was set at a value between 70-100 mbar. After plasma formed, argon pressure was decreased to 7 mbar by adjusting the gate valve, and the pressure was kept constant throughout the deposition process.

The prior deposition was initiated the substrate surfaces were cleaned further via bias sputtering carried out for 15-minute. After substrate cleaning, the targets were cleaned by operating them for 5 minutes while the shutters were closed.

3.1.1   Determination of Tooling Factor

So as to obtain deposited films with controlled thickness, it is necessary to determine a tooling factor. The tooling factor relates the readings made with the thickness monitor with the actual thickness of the film.
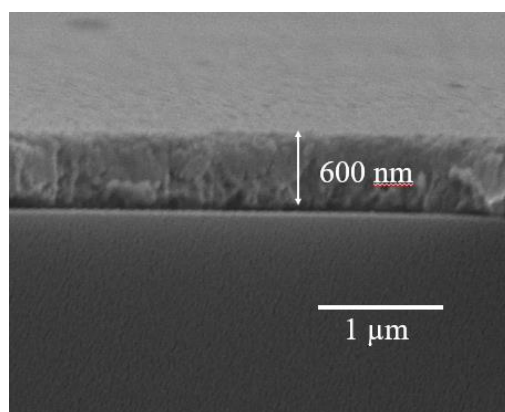
Figure 3.4. Representative example for Pd calibration thickness measurement by FE-SEM

First, a tooling factor of 100 was entered into the respective channel of the thickness monitor. For example, Pd (Gun 3) was loaded with a power of 25 W, and the deposition was carried out for 2 hours. Then the experiment was terminated, and the glass substrate close to Gun3 was broken and examined under SEM. An example given in Fig. 3.4 is quite typical and shows a film thickness of 600 nm. As a result, tooling of 166 was entered into channel three of the thickness monitor. By repeating these procedures, tooling factors were determined for each target.

3.2   Material Characterization

Structural characterizations of thin film membranes were carried out by X-ray diffraction using Bragg Brentano mode. The pattern was recorded using Cu-Kα radiation with a scanning speed of 2°/min rate Using Rigaku DMAX2200. Where necessary, the pattern was Rietveld refined using MAUD software. Deposited membranes were also examined in SEM (FEI Nova Nano 430). Chemical compositions of the membranes were determined in SEM using EDS analysis. For this purpose, the membrane was viewed under low magnification, and data was collected for 60 seconds (20 kV with a spot size of 6.0).

3.3   4-Probe Resistivity Measurement

Resistivity measurements were carried out with four-probe measurements. The set-up is shown in Figure 3.5. Resistivities of the samples are determined[66] first by determining the sheet resistance,

$$R_{Sheet} = \frac{V}{I} \cdot C\left(\frac{d}{s}\right)$$

Eqn. 3.1.

Where R_{sheet} is sheet resistance (Ω/sq), V is voltage (V), I is current (mA), d is the diameter of thin-film, and s is the distance between probes (cm). For the current experiments d= 1.8 cm and s= 0.35 cm. C is the correction factor that equals 3.4091 for the current values of d and s.

From sheet resistance, the resistivity is determined in units of (Ω.cm).

$$\rho = R_{Sheet} \cdot t$$

Eqn. 3.2.

Where t is the film thickness in cm.

The set-up incorporates a thin film four-probe holder, a gas-tight chamber placed inside a furnace, and a gas connection system. Thin film specimens are placed onto a holder with 47 mm diameter, as shown in Figure 3.5(b). The holder's position was adjusted with nuts so that there was good contact between the film and the electrodes. The Electrodes were gold-plated tungsten needles 2 mm in diameter with a pointed tip. The center-to-center distances between gold-plated needles were 3.5 mm. The electrodes, which had a length of 200 mm, were connected to electrical feedthrough at the top via gold-plated springs.

Having placed the film, the thin film four probe holder was placed inside the chamber and closed via nuts at its periphery using a copper gasket. The chamber at its flange had electrical feedthrough for the electrodes, a gas connection, and a thermocouple feedthrough. The chamber was placed inside the furnace, which had an internal bore of 80 mm. The temperature was monitored with a K-type thermocouple placed through the flange close to the thin film sample. The temperature of the furnace can be adjusted up to 500 °C.

The chamber can be connected to either argon or hydrogen and as well as to vacuum. The system incorporates a pressure transmitter that allows measurements up to 10 bars. The vacuum pump was Pfeiffer HiCube 80 Eco turbomolecular pump, which allowed measurements down to 1×10^{-6} mbar.

The measurements involved the following steps; First, the sample was placed in the holder, Figure 3.5(b), the position of the thermocouple was checked, and the CF flange at the top was tightened to make it gas tight, then the chamber was evacuated. Then the chamber is fed 1 bar of argon and evacuated by the vacuum system. This step was repeated three times. Then 1 bar of argon is fed to the system, and the chamber is heated to the desired temperature.

(a)

(b)

(c)
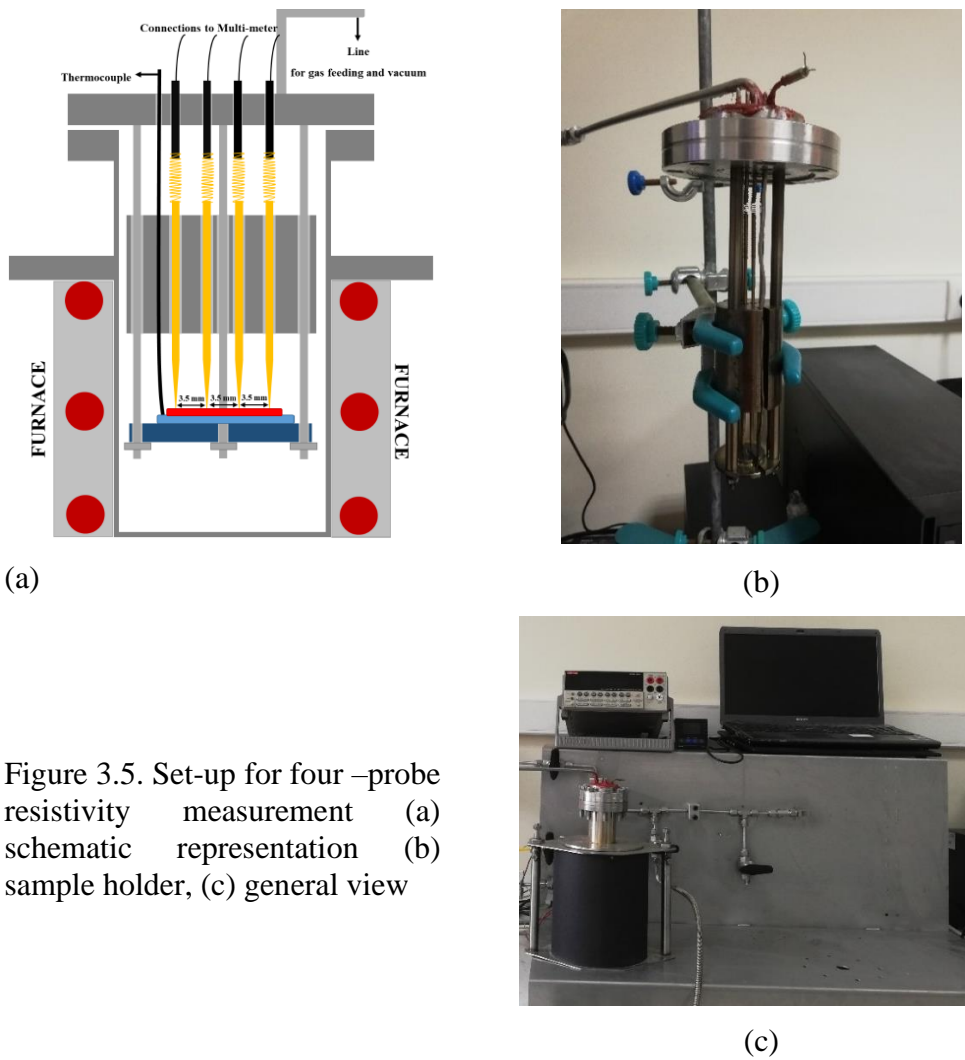
Figure 3.5. Set-up for four –probe resistivity measurement (a) schematic representation (b) sample holder, (c) general view

Electrical resistivity measurements are conducted using Keithley 2700 4 Probe Digital Multimeter. The setup allows a connection to a computer, and data collected can be followed with a module in Excel software. During measurement, 10 mA ± 5% current is applied through two outer electrodes while voltage value is measured through the inner two electrodes. According to the current input and voltage output, the sheet resistance of the film is obtained using Eqn. 3.1.

Resistivity measurements are carried out while the sample is heated (or cooled) by recording both the temperature and the resistivity Hydrogen reactivity index is defined as $\rho H_2/\rho Ar$ where ρH_2 and ρAr are resistivity of the film under hydrogen, and under argon, respectively both recorded at the same temperature.

3.4 Permeability Measurement

Hydrogen permeability of the membranes are measured using a setup shown in Fig. 3.6. Here measurements were based on equation given previously, Eqn. 2.9.

$$J = \frac{k}{x}\left(P_{Inlet}^{0.5} - P_{Outlet}^{0.5}\right)$$

Here, J is the hydrogen flux, P_{inlet} and P_{outlet} are inlet and outlet pressure, respectively, k is the permeability and x is the thickness of the membrane.

27
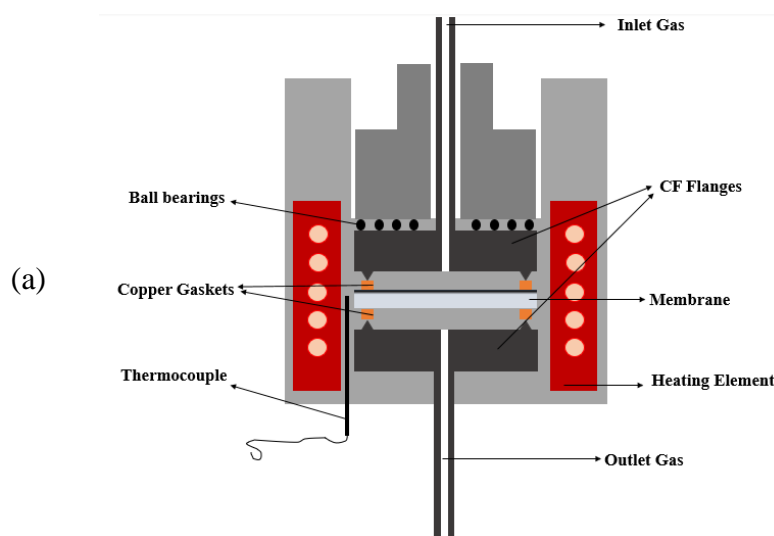
(b)
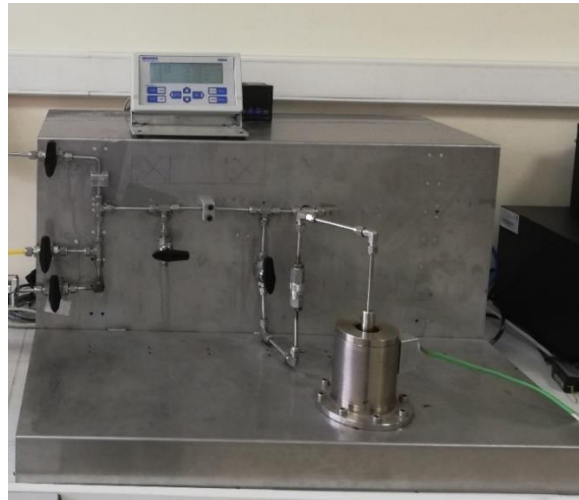
Figure 3.6. Permeability testing system's a) schematically representation b) the picture

Inlet and outlet pressures of the system are measured via pressure transmitters (Keller 21Y, 0-10 bar absolute). Gas fluxes are measured by Horiba Stec mass flow controller SEC-E400J (50 scc/min) monitored using Brooks Instruments reading unit (0254)

Permeability tests are conducted in the testing chamber where the membrane was placed in between two CF flanges. Two copper gaskets with 150 μm thickness were placed below and above the membrane. Clamping is carried out by screwing down the hollow nut above the top flange. This was achieved by ball bearings in a cage which decreases friction between screw and flange and facilitates tightening the hollow nut and, as a result, upper flange.

Membranes tested were 19 mm in diameter and provide 15 mm active area for hydrogen permeation. Temperature of the samples are controlled using a K-Type thermocouple located near the sample, Figure 3.6(a).

The set-up was placed inside a furnace, as shown in Figure. 3.6(b). The temperature inside the chamber can be increased up to 400 ºC by means of 330-Watt heating element.

Before the measurement, the system is checked for gas tightness using argon. Then argon discharged by means of vacuum pump, and hydrogen gas is fed into the system

at 1 bar. Once the steady state conditions are reached, the pressure both at the inlet side and outlet side were recorded, and the flux at the outlet side was recorded. These measurements were repeated at pressures with the interval of 0.5 bars up to 4 bars. Permeability of the membrane was calculated using Eqn. 2.9.

3.5 Vacuum Thermal Dealloying

The porous metallic substrates, which are used as a support material for separation membranes, were prepared by the vacuum thermal dealloying method. The setup used for this purpose is shown in Figure 3.7. This setup consists of a tubular furnace and a vacuum system. The furnace had a quartz tube with an external diameter of 48 mm with a wall thickness of 2 mm with 1000 mm in length. The furnace yields a uniform temperature zone of 60 mm.

Figure 3.7. Vacuum thermal dealloying setup

The setup was connected to a vacuum system incorporating a Leybold Turbovac 250i turbomolecular pump, backed up with an Ulvac rotary pump. The vacuum level is monitored with Alcatel Vacuum Gauge. The system can reach a vacuum level as low as 1×10^{-7} mbar. The connection to the vacuum system was made by stainless steel

adapter using two O-rings pressed against a quartz tube by a tightening screw ring. The adapter had a valve (1/4 inch) for argon connection at the entry side. At the exit side, the adaptor had a brass sintered filter so as to protect the turbomolecular pump from metal vapors. As a further precaution, the exit side of the brass filter was filled with cotton to trap metal vapor that the brass filter could not trap.

(a) (b)

Figure 3.8. Stainless steel mask for vacuum dealloying (a) bare, (b) loaded.

Sheets to be dealloyed were punched into 19 mm diameter disc. They were placed in the hot zone of the furnace. Mostly, however, they were loaded onto a unique masking holder, as shown in Figure 3.8. The masking holder was in the form of stainless steel discs in 40 mm diameter, having an internal bore of 10 mm. They could be tightened with the use of three bolts. They also had two guides where pyrex glass tubes were placed to center the unit inside the furnace. The purpose of this masking holder was to mask the disc so that it will dealloy in the central 10 mm area, the rest being shadowed by the stainless steel rings.

CHAPTER 4

COMBINATORIAL DEPOSITION OF Pd-Co-Ni THIN FILMS

4.1   Introduction

As reviewed in Chapter 2.3, hydrogen separation membranes may be chosen from one of the three groups: amorphous, b.c.c. and f.c.c. membranes. Although the former two groups have their advantages, they have not been implemented as separation membranes. We, therefore, made our selection from f.c.c. membranes as they can be processed in various forms tubes, foils, etc., due to their inherent ductility.

A ternary system Pd-Co-Ni was selected as this was expected to yield f.c.c. membranes over a wide compositional field. Here the elements Pd and Ni are f.c.c., Co is hexagonal at room temperature but transforms to f.c.c. at temperatures above 422 $^{\circ}$C. Figure 4.1 shows binary phase diagrams of Pd-Ni, Ni-Co, and Pd-Co. It is seen that there is complete solid solubility in Pd-Ni binary system. Ni-Co and Pd-Co binary systems are pretty similar in that f.c.c. phase extends over a wide range, up to approx. 60% Ni in Ni-Co and up to %40 Pd in Pd-Co Therefore, based on binary phase diagrams, it is expected that a more significant portion of the compositional field in the ternary diagram is likely to have f.c.c. structure.

(a)

(b)

(c)
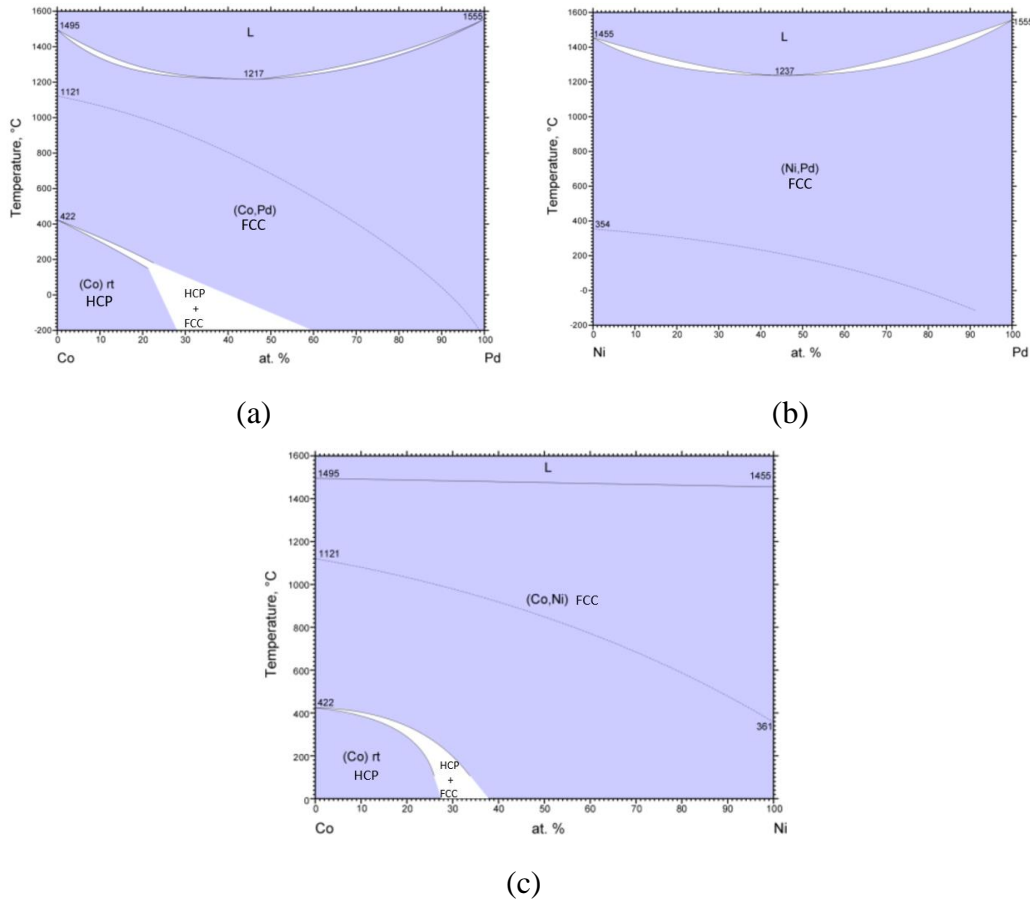
Figure 4.1. Phase diagram of (a) Co-Pd[67] (b) Ni-Pd[68] and (c) Co-Ni[69] binary systems

Hydrogen solubility of nickel and cobalt had been studied separately[70–72]. According to Santucci et. al. [70], Ni has solubility of $8x10^{-5}$ (H/M). That of Co is $3.65x10^{-5}$ (H/M)[72]. These values should be compared with that of Pd which has a value of $3x10^{-2}$ (H/M).

In the Pd-Co-Ni ternary system, several alloys were investigated as separation membranes. Zhang [42] studied Pd-5(at)%Ni and reported a permeability a permeability value of $3.1x10^{-6}$ mole/m^2.s.Pa at 500 ^{o}C. Suzuki et al[73] reports a value of $0.25x10^{-8}$ mole/m.sPa$^{0.5}$ for the same alloy and temperature. A ternary alloy with composition $Pd_{55}Ag_{28}Ni_{17}$ was studied by Piskin and Ozturk[44] where the permeability value was $6.50x10^{-10}$ mole/m.sPa$^{0.5}$.

4.2   Fabrication of Pd-Co-Ni Thin Film Membranes

4.2.1   Thin Film Production

Magnetron sputtering used for this study was described in detail in Chapter 3.1. Power settings and duration were selected to yield a film thickness of 600 nm in the three substrates nearest to the sputter targets. Power settings used for each target are reported in Table 4.1.

Table 4.1. Power settings and the deposition rates in sputter deposition of Pd-Co-Ni deposition. The rate refers to the substrates at each corner of the triangular sample magazine.

Target metal	Sputtering Gun	Power Applied (Watt)	Rate (Å/sec)
Ni	RF	33	0.9-1.0
Co	RF	115	0.9-1.0
Pd	RF	25	1.2-1.4

First, the deposition was carried out on glass substrates so as to determine the composition of the resulting thin films. A total of 21 glass substrates were used each 19 mm in diameter, Figure 3.3. Chemical composition determined with EDS analysis for each of the 21 thin films are reported in Table 4.2. The compositions are also shown plotted in Figure 4.2. It is seen that thin films cover a significant portion of the ternary field where Pd content varies from 15 at.% up to 85 at.%.

Having determined the chemical compositions. Sputter deposition was carried out with a new set of glass substrates. This was carried out with the same settings, but the duration was increased five times the previous value. As a result, a set of 3 μm thick membranes were obtained.
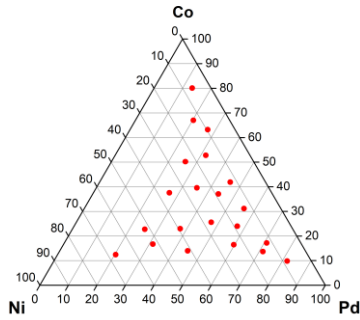
Figure 4.2. Composition distribution of sputter deposited thin films in Pd-Co-Ni
ternary diagram.

Table 4.2. Chemical composition of sputter deposited Pd-Co-Ni thin films

Sample No	Pd (at.%)	Co (at.%)	Ni (at.%)
1	13.3	80.1	6.6
2	20.3	67.0	12.7
3	27.2	63.2	9.6
4	25.9	50.2	23.9
5	31.8	52.8	15.4
6	45.8	41.9	12.3
7	26.6	37.5	35.9
8	35.2	39.6	25.2
9	44.0	37.1	18.9
10	55.9	31.2	12.9
11	25.4	22.7	51.8
12	37.7	23.0	39.3
13	47.2	25.6	27.2
14	57.2	23.9	18.9
15	70.9	17.1	12.0
16	20.4	12.4	67.2
17	31.3	16.7	52.0
18	37.6	51.0	11.4
19	59.7	16.4	23.9
20	71.4	13.6	15.0
21	81.8	9.8	8.4

4.2.2 Stabilization of Sputter Deposited Thin Films

Thin film membranes following depositions were subjected to a stabilizing heat treatment. For this purpose, thin film membrane was loaded into a chamber of a set-up shown in Figure 3.5 and heated under argon (1 bar initial pressure) to 450 °C with a heating rate of 3 °C/min while the resistivity was recorded. Figure 4.3 refers to a resistivity curve of $Pd_{47}Co_{26}Ni_{27}$ thin film. As seen in the curve, the resistivity, which rises with increasing temperature, having reached 170 °C shows a decrease that continues up to 300 °C and then shows little change with temperature up to 450 °C. Upon cooling the resistivity decreases consistently with the decrease in temperature.

The curve depicted in Figure 4.3 indicates that an annealing treatment at around 350 °C would be needed to stabilize the microstructure in the thin film. Considering that this temperature might change from film to film depending on the composition, a stabilization heat treatment was carried out at 450 °C for all deposited samples. The treatment was carried out under 1 bar of argon initial pressure heating rate was 3 °C/min to 450 °C, and the duration of treatment was 3 hours.
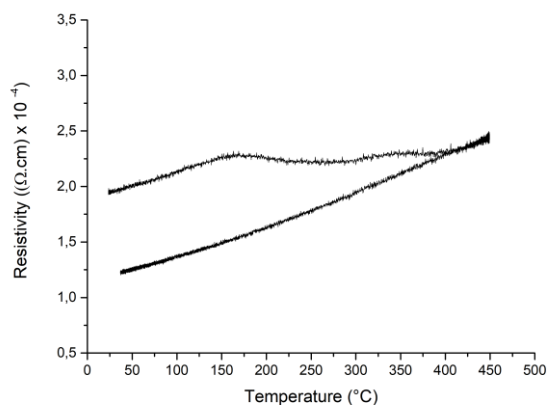
Figure 4.3. Resistivity curve in the as-deposited $Pd_{47}Co_{26}Ni_{27}$ while heating and cooling.
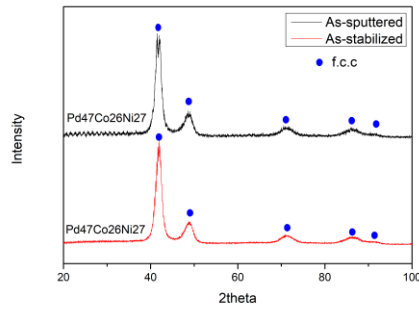
Figure 4.4. XRD plots of $Pd_{47}Co_{26}Ni_{27}$ for stabilized and sputtered conditions

Figure 4.4 shows the effect of stabilization treatment on the crystal structure. As can be seen, peak broadenings in stabilized conditions are slightly narrower than that of sputtered conditions, and a coarser structure was obtained. By looking at resistivity curves and X-ray diffraction patterns, it was concluded that the alloys were fully stabilized.

4.2.3 Structure of Thin Film Membranes

Starting from Co corner, the XRD patterns of three samples are show in Figure 4.5. The positions of the samples in the ternary diagram were also shown. It was seen that structure involves two phases h.c.p. and f.c.c. Peaks are quite broad in all samples.
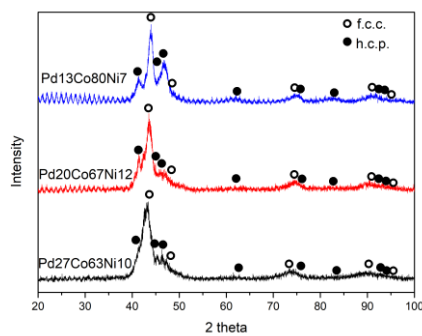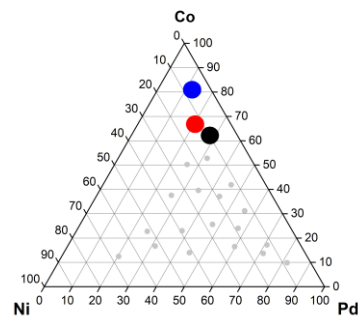
(a)   (b)

Figure 4.5. (a) X-ray diffraction patterns of deposited thin films $Pd_{13}Co_{80}Ni_7$, $Pd_{20}Co_{67}Ni_{12}$ and $Pd_{27}Co_{63}Ni_{10}$ and (b) their position in the ternary diagram.

36
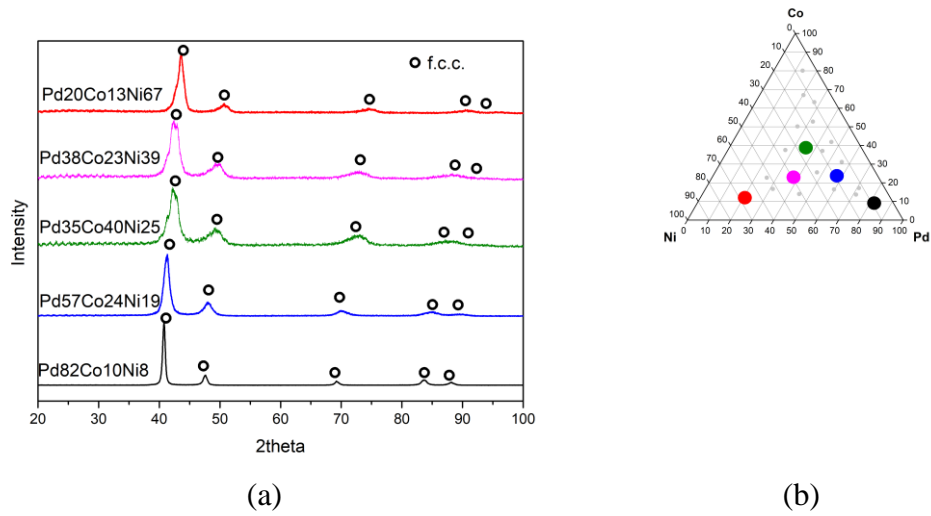
Figure 4.6. (a) X-ray diffraction patterns and (b) the position of the respective thin films $Pd_{35}Co_{40}Ni_{25}$, $Pd_{38}Co_{23}Ni_{39}$, $Pd_{57}Co_{24}Ni_{19}$, $Pd_{20}Co_{13}Ni_{67}$ and $Pd_{82}Co_{10}Ni_8$ in the ternary diagram compositions.

Table 4.3. Lattice parameter f.c.c. thin films in Pd-Co-Ni.

Pd (at.%)	Co (at.%)	Ni (at.%)	Lattice Parameters (Å)
20.37	12.42	67.21	3.613
25.42	22.75	51.83	3.622
26.63	37.51	35.87	3.638
31.26	16.69	52.04	3.648
37.71	22.99	39.30	3.680
35.21	39.56	25.22	3.694
44.81	13.98	41.21	3.720
47.24	25.56	27.20	3.744
44.02	37.06	18.91	3.751
45.78	41.87	12.36	3.769
59.74	16.43	23.83	3.781
57.20	23.95	18.85	3.792
55.93	31.15	12.92	3.799
71.34	13.65	15.01	3.811
70.89	17.14	11.97	3.815
81.76	9.79	8.45	3.836

XRD patterns of representative samples away from Co corner are given in Figure 4.6. All patterns are compatible with f.c.c. structure, though the lattice parameter changes over a relatively large range. The lattice parameters of the f.c.c. thin films are tabulated in Table 4.3. Here the values were determined via Rietveld refined XRD patterns using MAUD software. Thin films are tabulated with increasing value of the lattice parameter. It is seen that the parameter increases with increasing Pd content. The smallest measured lattice constant among the deposited films was a=3.613 Å for $Pd_{20}Co_{13}Ni_{67}$, and the largest was close to the Pd corner with 3.836Å for $Pd_{82}Co_{10}Ni_8$. It may be mentioned that the lattice parameter of pure palladium is a=3.889 Å is significantly larger than that of Nickel where a=3.524 Å. Thus, the larger lattice parameter obtained close to the Pd corner is quite compatible with these values.

As it can be seen, all of the samples except for the cobalt-rich corner have a face centered cubic structure. The choice of Pd-Co-Ni is therefore well justified as it can yield membranes over a wide compositional range. The lattice parameter can be varied over a wide range, the largest of which in the current membranes was a= 3.836 Å belonging to $Pd_{82}Co_{10}Ni_8$ composition.

4.2.4   Screening of Pd-Co-Ni Thin Films via Resistivity Measurement

Thin film membranes having passed the stabilization heat treatment were loaded into the setup, and following the required procedure, 1 bar of argon was admitted to the chamber. The resistivity was continuously measured while the film was heated to 450 °C with a heating rate of 3 °C/min and having reached the temperature cooling cycle was initiated where the cooling rate was again 3°C/min. However, the actual cooling rate was slower than this value.

Having reached the room temperature, argon was evacuated, and hydrogen was admitted to the chamber. The pressure in the chamber was again 1 bar, and the measurement was repeated with the same heating and cooling conditions.

Some samples at Co corner, e.g., sample $Pd_{13}Co_{80}Ni_7$ has failed due to the fact that the thin film membranes were broken into pieces during the measurements. This case was also seen for the samples $Pd_{32}Co_{53}Ni_{15}$ and $Pd_{46}Co_{42}Ni_{12}$. Therefore, resistivity measurements could not be conducted for these samples.

(a)   (b)

(c)
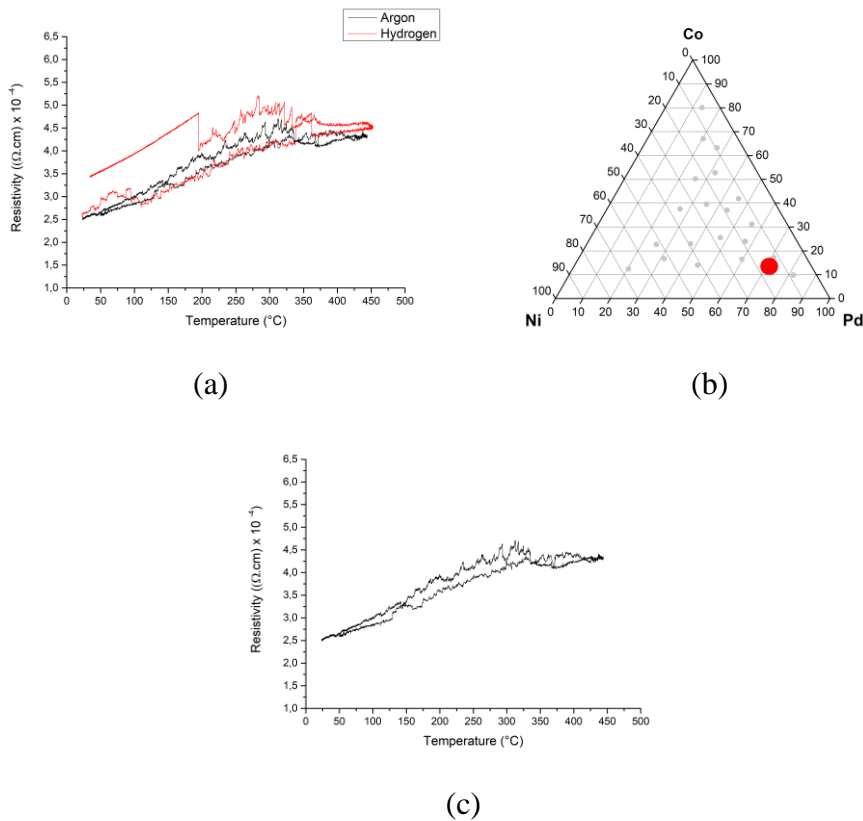
Figure 4.7. (a) Resistivity measurements of $Pd_{71}Co_{14}Ni_{15}$ and (b) position in the ternary diagram (c) resistivity measurement under argon for $Pd_{71}Co_{14}Ni_{15}$.

There was also another region in the diagram where thin film membranes showed signs of brittleness. Figure 4.7 refers to resistivity curve of $Pd_{71}Co_{14}Ni_{15}$ for the heating and cooling cycle. This sample is located further down in the ternary diagram close to the Pd corner. The curves follow each other in a similar path for heating and cooling. However, there are sudden jumps and irregularities in the resistivities. Looking at the argon curve, the resistivity increase with temperature stops at around 320 ºC. After this temperature, irregularities in resistivity were reduced, and the curve was flatter than the previous part. Similarly, resistance curves are quite smooth while heating from room temperature to 100 ºC and cooling from 100 ºC to room

temperature. This may be due to a phase transformation occurring between 100 ºC to 300 ºC,

Similar irregularities were also observed for the compositions near $Pd_{71}Co_{14}Ni_{15}$. These are $Pd_{71}Co_{17}Ni_{12}$ and $Pd_{56}Co_{31}Ni_1$, Figure 4.8.

(a)

(b)
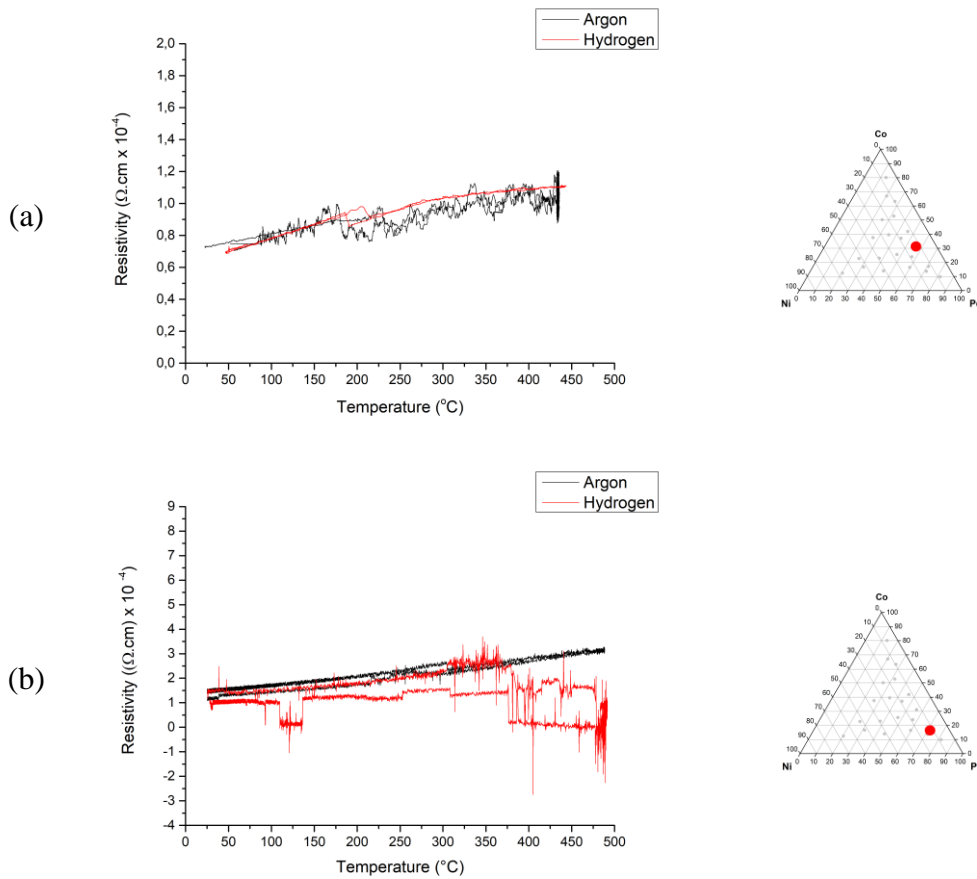
Figure 4.8. Compositions showing irregularities in their resistance curves for (a) $Pd_{56}Co_{31}Ni_{13}$ and (b) $Pd_{71}Co_{17}Ni_{12}$.

The resistivity curves for $Pd_{71}Co_{17}Ni_{12}$, as shown in Figure 4.8(a), depict a similar trend. There is a sudden drop in resistivity at 170 ºC during heating and a sudden jump at 210 ºC during cooling in the hydrogen curve. There are similar changes in the argon curve. This may strengthen the possibility of a phase transformation in this region. For the case of $Pd_{56}Co_{31}Ni_{13}$, the argon curve is smoother than that of hydrogen. Figure 4.8 (b). It should be noted that there are intense scatters in the hydrogen curve, which gives the impression that irregularities may be caused by

measurement difficulties rather than phase transformation. Further work would be necessary to identify the causes of these irregularities occurring in membranes with compositions at and around $Pd_{60}Co_{20}Ni_{20}$.
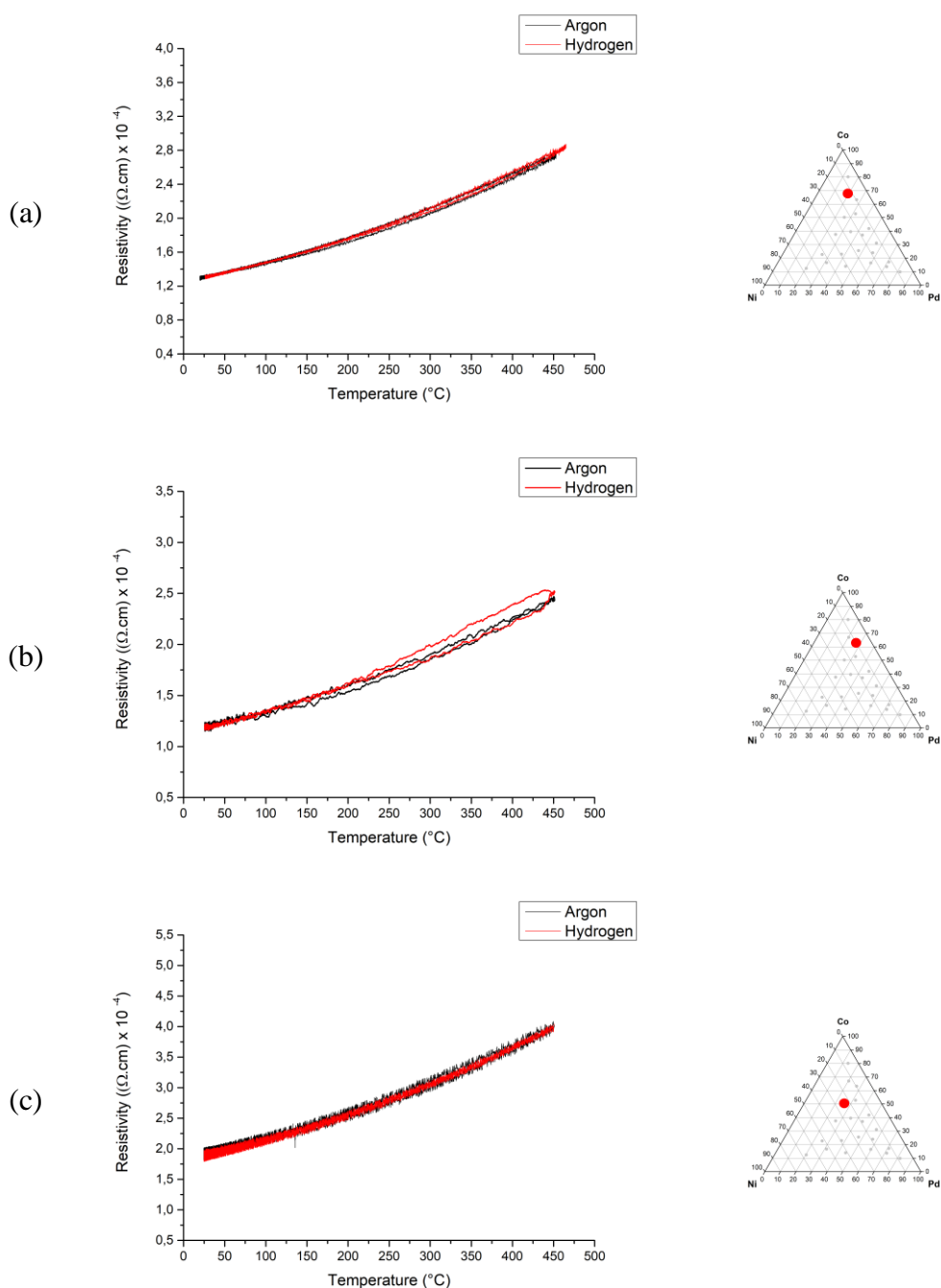
Figure 4.9. Resistivity measurement plots and their positions in ternary for the compositions of (a)$Pd_{20}Co_{67}Ni_{13}$ (b)$Pd_{27}Co_{63}Ni_{10}$ (c)$Pd_{26}Co_{50}Ni_{24}$ compositions

Figure 4.9 shows the resistivity curves of samples in the upper part of the ternary diagram. The curves under hydrogen and argon are smooth in the temperature range 20 ºC-450 ºC. Moreover, the resistivity curves taken under argon and hydrogen are almost the same, implying no differences in how the sample interacts with argon and hydrogen. The fact that the resistivity curve under hydrogen does not deviate from that of argon indicates that the sample does not have hydrogen solubility. Thus, under the conditions used in the present study, i.e., temperature up to 450 ºC and 1 bar of hydrogen pressure, these membranes are unsuitable for hydrogen separation.

(a)

(b)
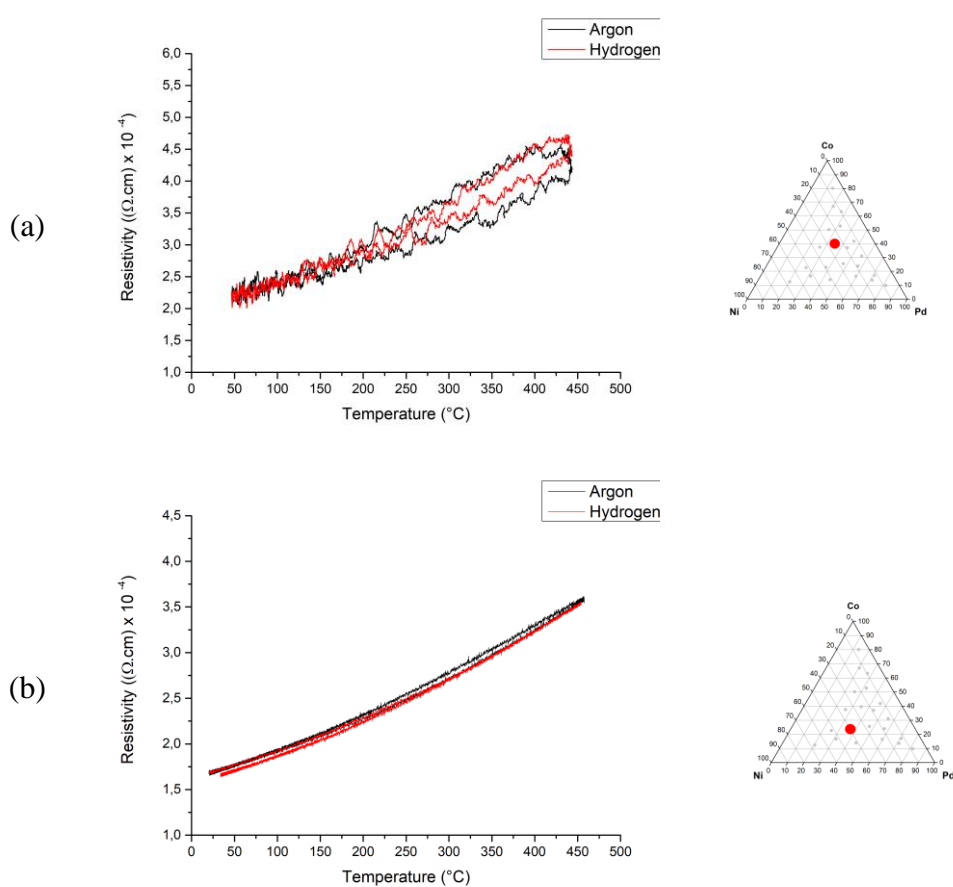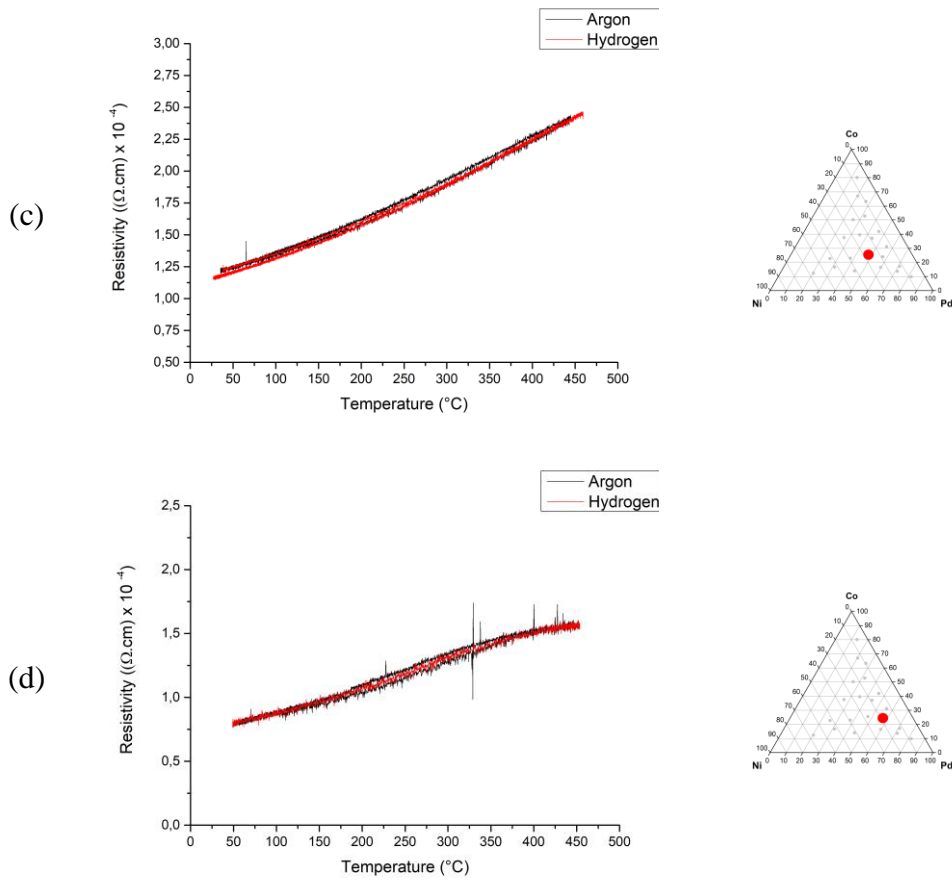
Figure 4.10. Resistivity measurement plots belonging (a) $Pd_{35}Co_{40}Ni_{25}$, (b) $Pd_{38}Co_{23}Ni_{39}$, (c) $Pd_{47}Co_{26}Ni_{27}$, (d) $Pd_{57}Co_{24}Ni_{19}$ compositions

The resistivity measurements taken from the mid-compositions in the ternary diagram, $Pd_{35}Co_{40}Ni_{25}$, $Pd_{38}Co_{23}Ni_{39}$, $Pd_{47}Co_{26}Ni_{27}$, and $Pd_{57}Co_{24}Ni_{19}$ are given in Figure 4.10. These curves are similar to those reported above in that the resistivity. Under hydrogen are identical to those taken under argon, indicating that the compositions do not react with hydrogen under the current experimental conditions.
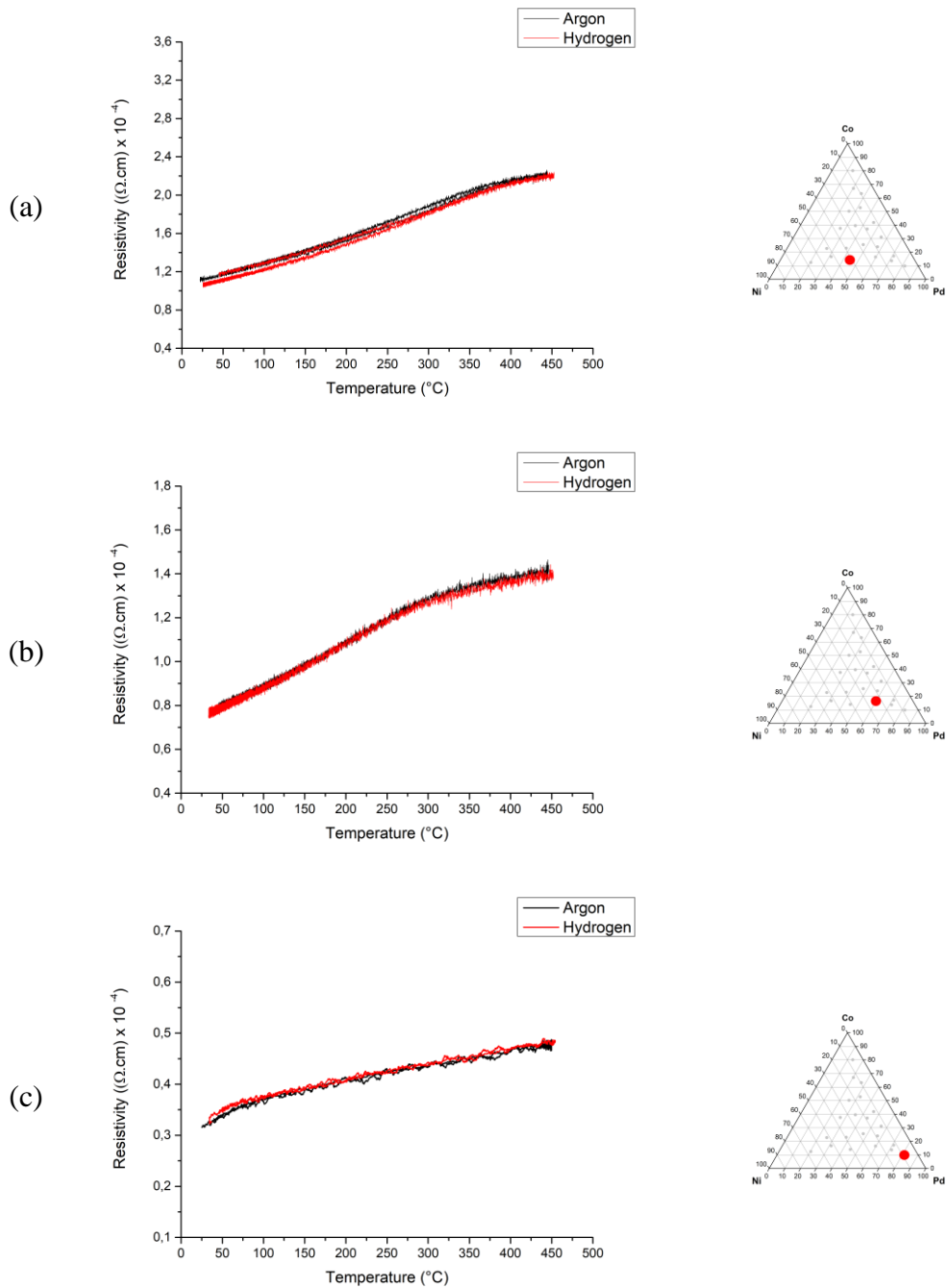
Figure 4.11. Resistivity measurement plots and their positions in ternary for (a) $Pd_{45}Co_{14}Ni_{41}$, (b) $Pd_{60}Co_{16}Ni_{24}$, (c) $Pd_{82}Co_{10}Ni_8$ Pd-rich compositions

Figure 4.11 shows curves for $Pd_{45}Co_{14}Ni_{41}$, $Pd_{60}Co_{16}Ni_{24}$, and $Pd_{82}Co_{10}Ni_8$ lower down in the ternary diagram. The curves were found to be similar to those reported above. Even when the palladium content reached 82%, the curves under hydrogen

44

did not differ from those recorded under argon, i.e., there is no solubility of hydrogen in these samples.

Thus, it can be concluded that as far as the compositional field covered in this work, and for the current conditions of temperature up to 450 $^{\circ}$C 1 bar of hydrogen pressure, there are no compositions in Pd-Co-Ni ternary system that appear to be suitable as candidate for hydrogen separation membrane.

CHAPTER 5

COMBINATORIAL DEPOSITION OF Pd-Mn-Ag THIN FILMS

5.1 Introduction

This chapter examines the ternary system, Pd-Mn-Ag. There is no ternary phase diagram of this system. The binary phase diagrams are reported in Figure 5.1.

(a)

(b)

(c)
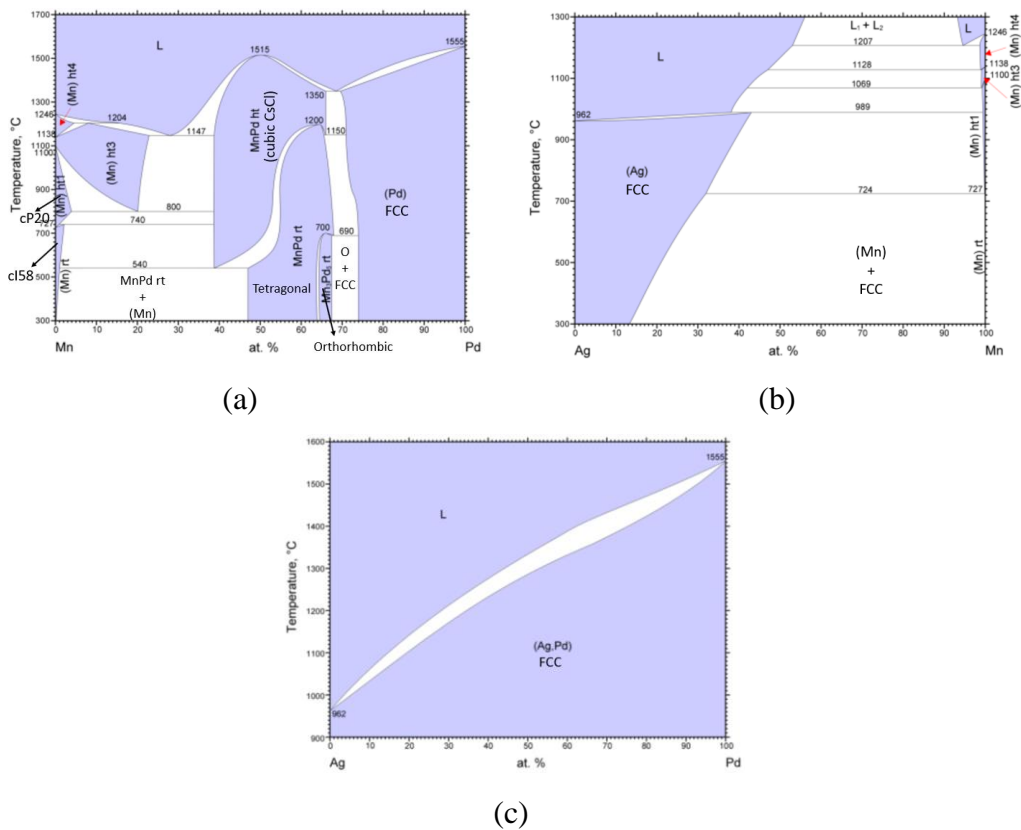
Figure 5.1. Phase diagram of (a) Mn-Pd[74], (b) Ag-Mn[75] and (c) Ag-Pd[76] binary systems

It is seen that Pd-Ag binary phase diagram shows complete solubility and forms f.c.c. structure. In Pd-Mn, f.c.c. solid solution extends up to approximately 25 at.% Mn where it joins two phase region comprising Mn_3Pd_5 intermetallic. In the case of Ag-

Mn diagram, f.c.c. phase is quite narrow as the solubility of Mn in Ag is not more than approximately 10 at.% Mn.

The binary phase diagrams given above are such that we can expect f.c.c. phase field towards the Pd-Ag line in the ternary diagram. It may added that the well-known commercial composition $Pd_{77}Ag_{23}$ (at.%) [3] is contained in this ternary diagram which yields a permeability of 3.21×10^{-8} mole/m.s.$Pa^{0.5}$ at 350 ^{o}C [39].

5.2   Fabrication of Pd-Mn-Ag Thin Film Membranes

5.2.1   Thin Film Production

To cover whole ternary system, two experiments were carried out. Details of calibrations about the determination of the tooling factor were given in Chapter 3. Power settings used in the depositions are reported in Table 5.1 and

Table 5.2, respectively.

Table 5.1. Sputtering parameters for Pd-Mn-Ag thin film deposition

Target Metal	Sputtering Gun	Power Applied (W)	Deposition Rate (Å/Sec)
Pd	RF	16	2.0-2.1
Mn	RF	35	2.0-2.1
Ag	RF	18	2.0-2.1

Table 5.2. Sputtering parameters for Pd-Mn-Ag thin film deposition

Target Metal	Sputtering Gun	Power Applied (W)	Deposition Rate (A/Sec)
Pd	RF	15	2.1-2.2
Mn	RF	33	1.8-1.9
Ag	RF	17	2.1-2.2

(a)   (b)
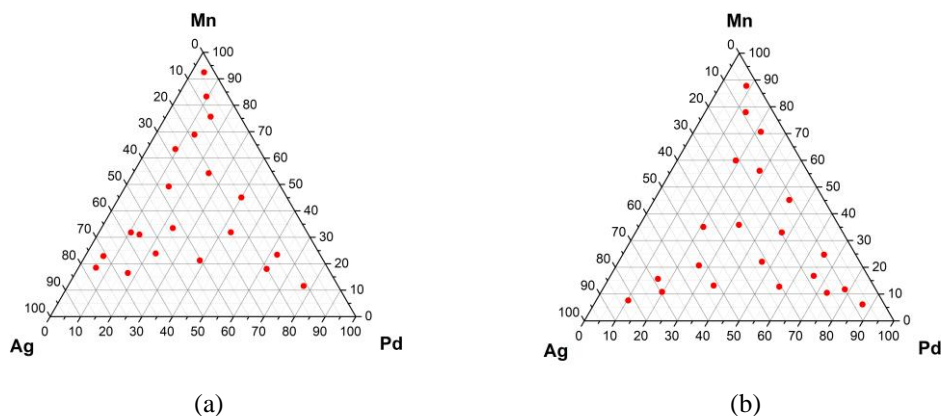
Figure 5.2. The position of thin film membranes in the Pd-Mn-Ag ternary diagram. (a) first set, (b) second set see Table 5.1 and

Table 5.2.

Thin film membranes deposited on glass substrates were analyzed with EDS. For every membrane, 5 measurements were taken under 200x magnification with 60 second measurement time, applied voltage and spot size was 20 kV, and 6.0, respectively. The chemical compositions of the films are shown separately in Figure 5.2 (a) and (b). It can be seen that the composition distribution, which tended to be close to the Ag-Mn line in the first experiment shifted to the Pd-Ag line in the second experiment. It is seen that the distributions complement each other and enable a wide compositional range to be covered in the ternary diagram. The two set of thin film samples are combined together in Table 5.3, where there are a total of 42 thin film membranes. The positions of these thin film membranes are indicated in the ternary diagram given in Figure 5.3.

Table 5.3. Compositions of thin film membranes in Pd-Ag-Mn.

Sample no	Pd (at.%)	Mn (at.%)	Ag (at.%)	Sample no	Pd (at.%)	Mn (at.%)	Ag (at.%)
1	4	93	3	22	8	88	4
2	5	88	7	23	13	78	9
3	10	83	7	24	22	70	8
4	9	63	28	25	19	60	21
5	13	69	18	26	29	56	15
6	15	75	10	27	44	45	11
7	10	32	58	28	21	35	44
8	14	49	37	29	32	36	32
9	25	54	21	30	47	33	20
10	40	45	15	31	65	25	10
11	6	23	71	32	16	16	68
12	14	31	55	33	27	20	53
13	23	34	43	34	46	22	32
14	43	32	25	35	66	17	17
15	63	23	14	36	78	12	10
16	6	18	76	37	10	8	82
17	17	17	66	38	20	11	69
18	23	24	53	39	35	13	52
19	38	21	41	40	57	13	30
20	62	18	20	41	73	11	16
21	77	12	11	42	87	6	7
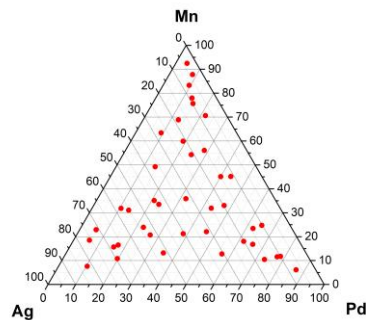
Figure 5.3. Composition distributions of 42 different samples obtained from two different deposition process.

5.2.2   Stabilization of Sputter Deposited Thin Films

Stabilization treatments were conducted in the same way as was explained in Chapter 4.2.2.

Figure 5.4 refers to a typical example, $Pd_{35}Mn_{13}Ag_{52}$. There is little change in resistivity up to 200 °C. There is a marked decrease it the resistivity from 200°C to 250 °C. Above that point, there is a linear reduction in resistivity from 250 °C. to 450 °C. Unlike the curve in the previous system, here, the curve does stabilize at a constant value of resistivity, see Figure 4.3. For this reason, stabilizing treatment made use of a different practice. The samples were heated to 450 °C but kept at that temperature for 7 hours to minimize changes that could occur in subsequent evaluation. The cooling curve, as seen in

Figure 5.4, is relatively smooth with a substantial decrement in resistivity as compared to as-deposited sample.

(a)

(b)
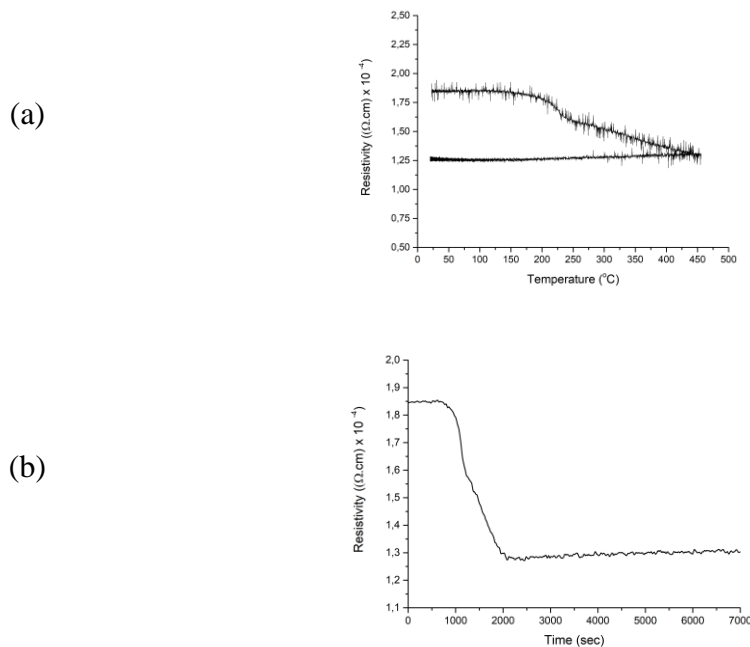
Figure 5.4. Resistivity measurement taken during stabilization of $Pd_{35}Mn_{13}Ag_{52}$. The sample was annealed 7 hours at 450 ^oC. (a) Resistivity versus temperature (b) resistivity versus annealing time at 450 ^oC.
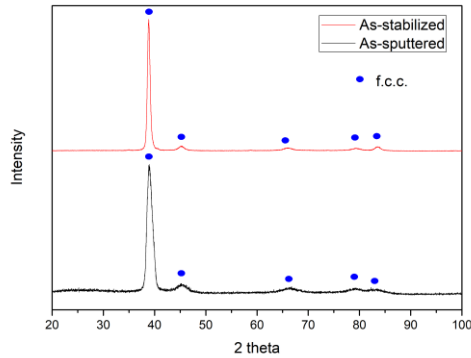
Figure 5.5. X-ray diffraction patterns of as sputtered and as stabilized condition of $Pd_{35}Mn_{13}Ag_{52}$.

Figure 5.5 shows the effect of stabilization treatment on crystal structure. As it is seen, peak broadenings are narrower than that of as sputtered sample. This implies that the sample after stabilization treatment are not as fine as the sputtered sample.

5.2.3 Structure of Thin Film Membranes

(a)   (b)
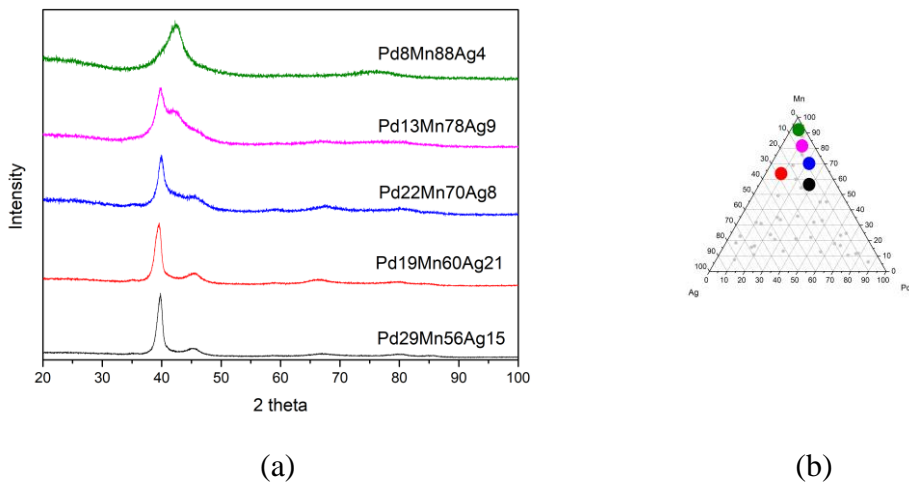
Figure 5.6. X-ray diffraction patterns of Mn rich samples in Mn-Pd-Ag ternary diagrams. The patterns refer to samples in as sputtered condition. (b) positions of the compositions in the ternary diagram.

52

X-ray diffraction patterns of samples in the Mn corner of the ternary diagram are given in Figure 5.6. Here, peaks are quite broad, and samples may even be amorphous. Figure 5.7 shows the peak positions of α-Mn, which has body centered cubic structure comprising 58 atoms per unit cell, i.e., cI58 in Pearson Symbol. It is seen that α-Mn has its strongest peak at ≈ 43° and there are also additional peaks in the vicinity from 2θ= 40° to 52°. The position of broad peaks in the Mn corner of the ternary diagram matches the peak positioning of α-Mn as the individual peaks merge into one another due to pronounced peak broadening.
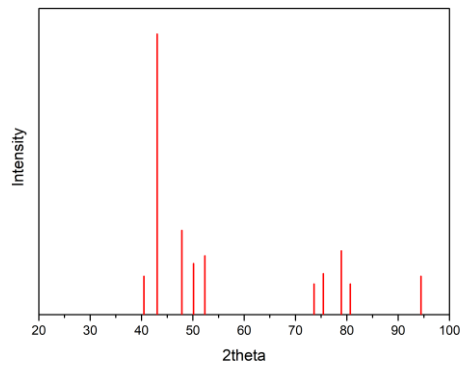
Figure 5.7. X-ray diffraction of α-manganese [77]

(a)   (b)

Figure 5.8 (a) X-ray diffraction patterns of mid-zone compositions. The patterns refer to samples in as sputtered condition. (b) positions of the compositions in the ternary diagram.

53

Figure 5.8 (a) X-ray diffraction patterns of mid-zone compositions shows X-ray diffraction patterns of samples towards the middle of Pd-Mn-Ag phase diagram. The strongest peak in this diagram occurs at $2\theta \approx 40^\circ$. This phase is consistent with an f.c.c. structure which accounts for a fraction of peaks in the diagram. These peaks are shown with an open symbol in Figure 5.8. There are a set of remaining peaks in the pattern whose intensity is much less than the previous. These are marked with a filled symbol. Thus, there are more than a single phase in these samples. The peak positioning of the minor phase was compared to possible intermetallics in Pd-Mn system. The intermetallics, MnPd[78,79] Mn3Pd5[80], as well as Mn7Pd9[78] MnPd3[81], were checked if they have a peak at approximately $2\theta=35^\circ$. Unfortunately, none of the intermetallics matched with this peak positioning. It may be mentioned that the peak positions of this minor phase appear compatible with an f.c.c. structure with a relatively large lattice parameter (a> 4.44). Further study is needed to fully identify this minor phase.

Patterns in Figure 5.8 are ordered such a manner that the strongest peak of the major f.c.c. phase shifts towards the left, i.e., lattice parameter increases from top to bottom. It is seen that this correlates with the Ag content of the samples, i.e., lattice parameter increases with increasing silver content.

(a)   (b)

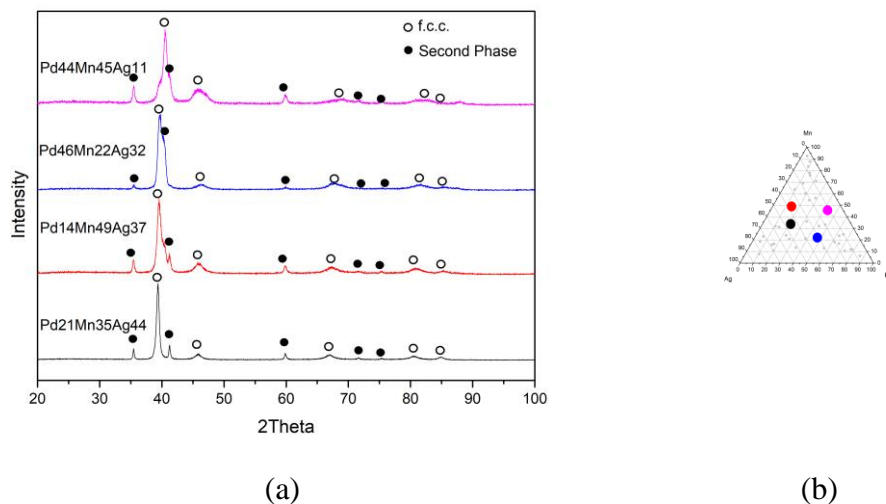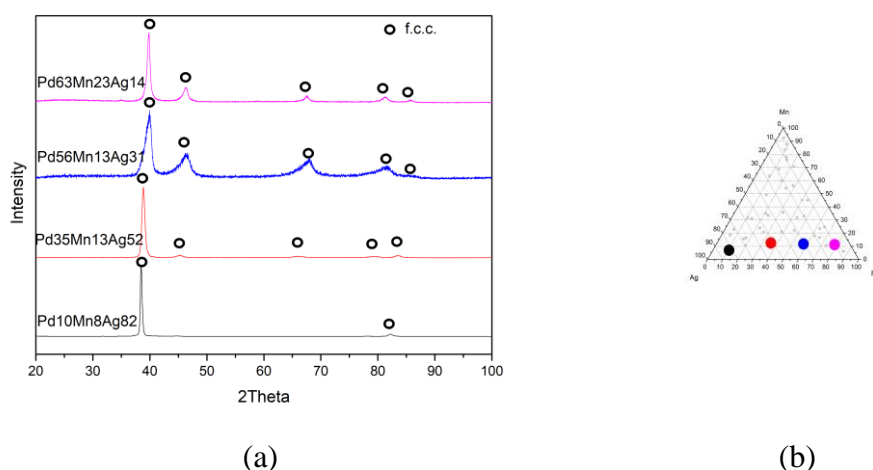Figure 5.9. (a) X-ray Diffraction Patterns for the compositions on Pd-Ag line. The patterns refer to samples in as sputtered condition. (b) positions of the compositions in the ternary diagram.

X-ray diffraction patterns of samples close to Pd-Ag line are given in Figure 5.9. It is seen that the structure there is only the primary f.c.c. phase in these samples. Here, compositions contain less than 20% manganese. Peak positions shift to the right as compositions get richer in Pd content. The fact that Pd has a lattice parameter of 3.889 Å and that of Ag is 4.091 Å are consistent with these peak shifts.
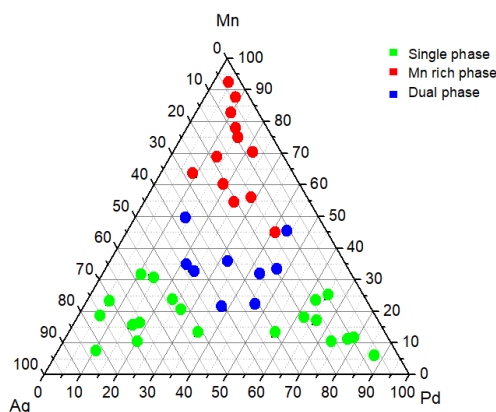
Figure 5.10. Phase make-up of thin film samples in Pd-Ag-Mn ternary diagram. Thin films with single phase f.c.c. structure are shown with green symbols.

Collecting all observations reported above, there are three distinct areas in the Pd-Ag-Mn phase diagram, Figure 5.10. Red legends show samples with Mn-rich phase. Blue represents the dual phase region where the primary phase is f.c.c. and green legends represents regions with the single phase f.c.c. structures.

Since for the purpose of the current work, samples with f.c.c. structure are important, all samples comprising a primary f.c.c. phase are analyzed further with Rietveld refinement. Lattice parameters obtained with this refinement are given in Table 5.4. Here the samples are listed in the order of increasing lattice parameter.

It is seen that there is a good correlation between the lattice parameter and the silver content of the samples. Thus, as the lattice parameter increases, the silver content of the sample increases. The case is reverse for Pd, i.e., as Pd content increases, there is a decrease in the lattice parameter. Knowing that the pure silver and palladium have lattice parameters of 4.091Å and 3.889 Å, respectively, changes in the lattice parameter of the samples are consistent with these values.

Table 5.4. Lattice constants for single phase Pd-Mn-Ag alloys

Compositions (at.%)	Lattice Parameters (Å)
$Pd_{87}Mn_6Ag_7$	3.893
$Pd_{63}Mn_{23}Ag_{14}$	3.896
$Pd_{77}Mn_{12}Ag_{11}$	3.906
$Pd_{65}Mn_{25}Ag_{10}$	3.908
$Pd_{73}Mn_{11}Ag_{16}$	3.909
$Pd_{62}Mn_{18}Ag_{20}$	3.911
$Pd_{56}Mn_{13}Ag_{31}$	3.920
$Pd_{66}Mn_{17}Ag_{17}$	3.922
$Pd_{20}Mn_{11}Ag_{69}$	3.985
$Pd_{35}Mn_{13}Ag_{52}$	3.999
$Pd27Mn_{20}Ag_{53}$	4.033
$Pd_{17}Mn_{17}Ag_{66}$	4.038
$Pd_6Mn_{23}Ag_{71}$	4.048
$Pd_{10}Mn_8Ag_{82}$	4.070
$Pd_{16}Mn_{16}Ag_{68}$	4.074

5.2.4 Screening of Pd-Mn-Ag Thin Films via Resistivity Measurement

First, thin film samples close to the Mn corner are evaluated regarding resistivity measurement. Unfortunately, these membranes were very fragile, and surface cracks occurred during the test. Therefore, it was not possible to take resistivity measurements from these samples.

          (a)   (b)
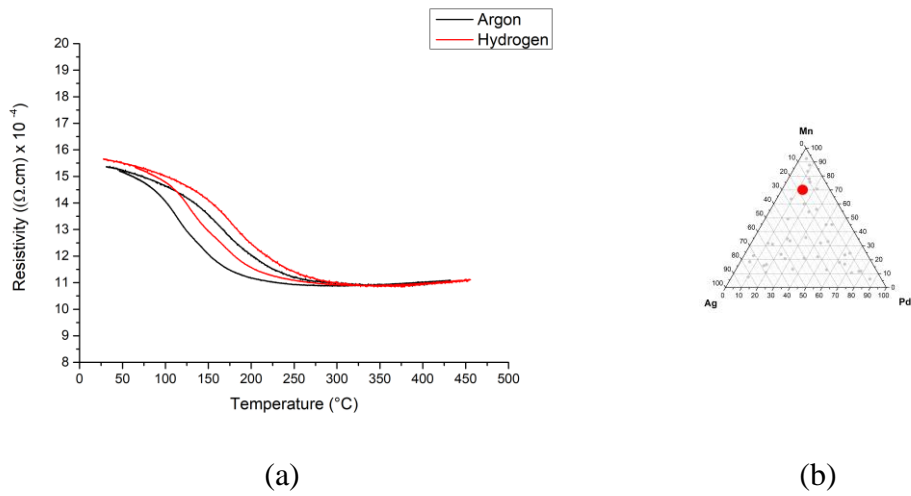
Figure 5.11. (a) Resistivity measurement plot and (b) $Pd_{13}Mn_{69}Ag_{18}$ composition's location in the ternary diagram.

Figure 5.11 shows a sample not too far off the Mn corner where the measurement was possible. The sample had a composition of $Pd_{13}Mn_{69}Ag_{18}$. It is seen that resistivity decreased with increasing temperature, both in argon and hydrogen. Upon cooling, the reverse takes place. There is, however, a small shift in each curve.
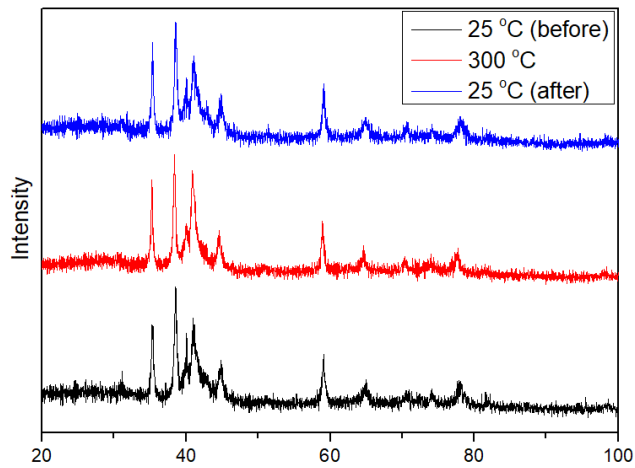
Figure 5.12. high temperature X-ray diffraction of membrane $Pd_{13}Mn_{69}Ag_{18}$

Crystal structure of $Pd_{13}Mn_{69}Ag_{18}$ membrane was examined with high temperature X-ray diffractometry. Figure 5.12 shows the XRD patterns recorded at room temperature, at 300ºC, and back to room temperature again. The patterns are very similar to one another, implying a structural change in the sample upon heating.
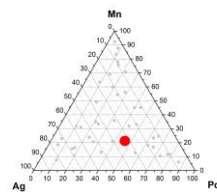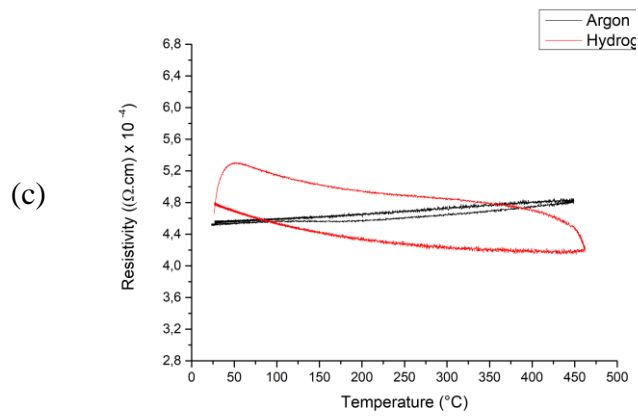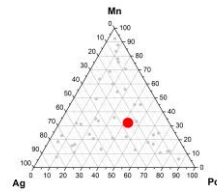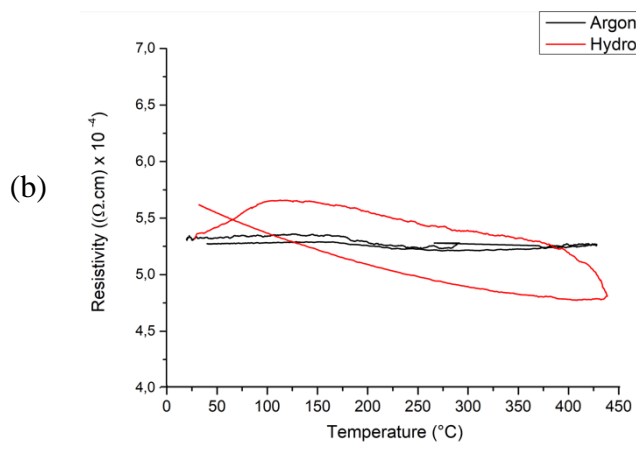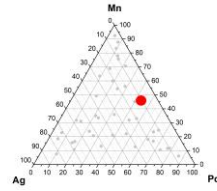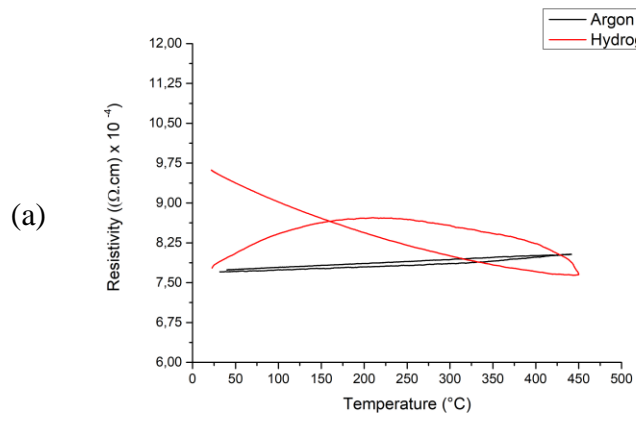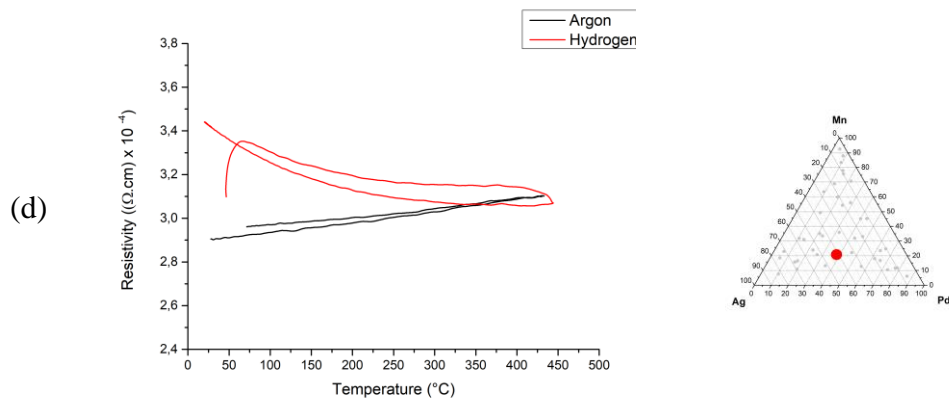
Figure 5.13. Resistivity vs Temperature curves of (a)$Pd_{44}Mn_{45}Ag_{11}$, (b)$Pd_{43}Mn_{32}Ag_{25}$, (c)$Pd_{46}Mn_{22}Ag_{32}$, (d)$Pd_{38}Mn_{21}Ag_{41}$ and their compositions in the ternary diagram.

Then samples in the mid region of the ternary diagram were investigated. Samples with relatively high the Mn content fragmented during heating therefore, reliable measurements could not be taken from some of these membranes. Representative samples from which measurements were taken are given in Figure 5.13. Here patterns refer to samples $Pd_{44}Mn_{45}Ag_{11}$, $Pd_{43}Mn_{32}Ag_{25}$, $Pd_{46}Mn_{22}Ag_{32}$ and $Pd_{38}Mn_{21}Ag_{41}$. They display similar curves. The curves recorded under hydrogen are quite different compared to those recorded under argon.

For the compositions given in Figure 5.13, the resistivity curves under argon are quite similar to each other. While in $Pd_{44}Mn_{45}Ag_{11}$ and $Pd_{43}Mn_{32}Ag_{25}$, the curves are quite flat, in $Pd_{46}Mn_{22}Ag_{32}$ and $Pd_{38}Mn_{21}Ag_{41}$ the curves have higher slopes. The display resistivities are much less than those measured under argon at the same temperature. Upon cooling, the resistivity rises continuously and remains high at room temperature. In the latter two samples, the resistivity peaks as soon as they are exposed to hydrogen, decreasing with increasing temperature. Upon cooling, the resistivity rises but at some distance below the heating curve.

Resistivity measurements were followed by single phase region. As stated previously, this region falls on the Pd-Ag line. Unlike other regions, measurements taken from these regions did not result in the fragmentation of the thin films or

59

peeling from the substrate. Therefore, more measurements were able to be conducted.

(a)

(b)

(c)

(d)
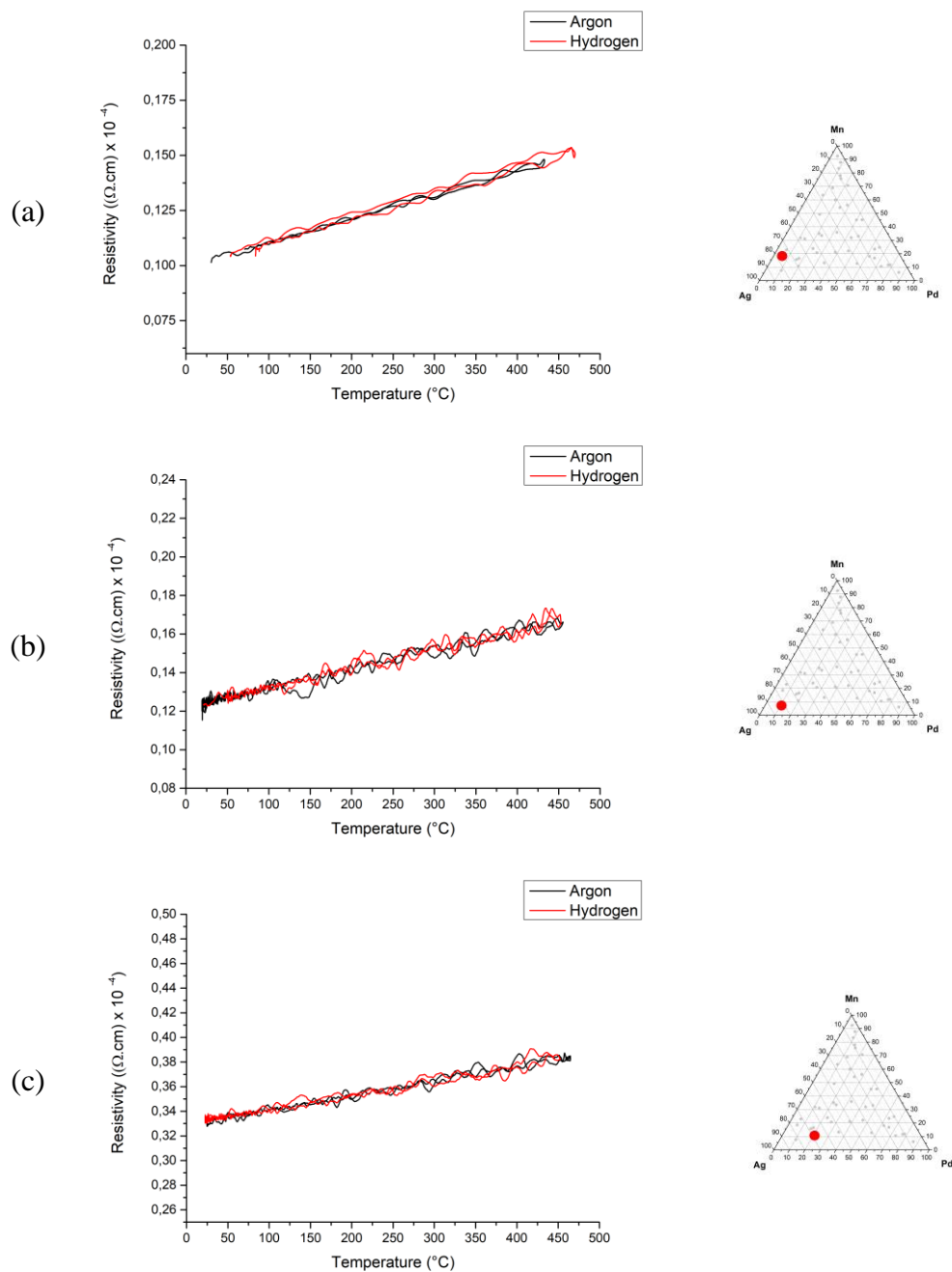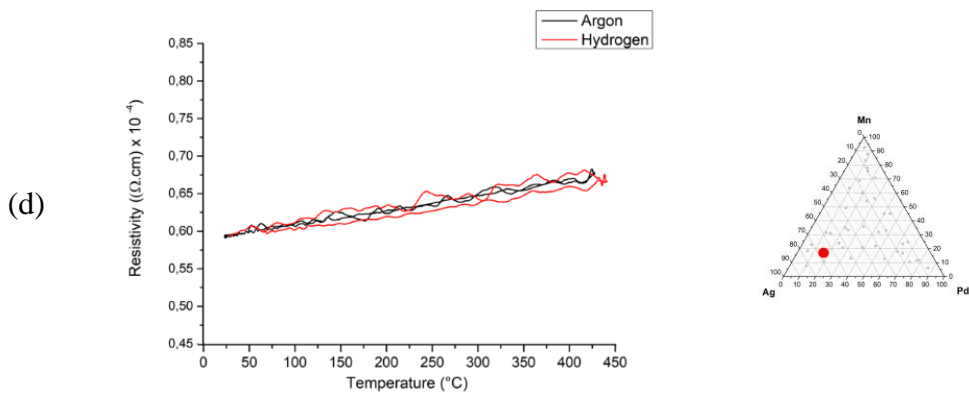
Figure 5.14. Resistivity measurement plots of Ag Rich compositions of (a) $Pd_6Mn_{18}Ag_{76}$, (b) $Pd_{10}Mn_8Ag_{82}$, (c) $Pd_{20}Mn_{11}Ag_{69}$, (d) $Pd_{17}Mn_{17}Ag_{66}$ and their positions in the ternary diagram.

Figure 5.14 shows resistivity measurements of samples close to the Pd-Ag line. It is seen that curves obtained under hydrogen and argon are almost the same, implying that none of these samples react with hydrogen under the current conditions, i.e., there is no solubility of hydrogen in these samples.

(a)

(b)

(c)
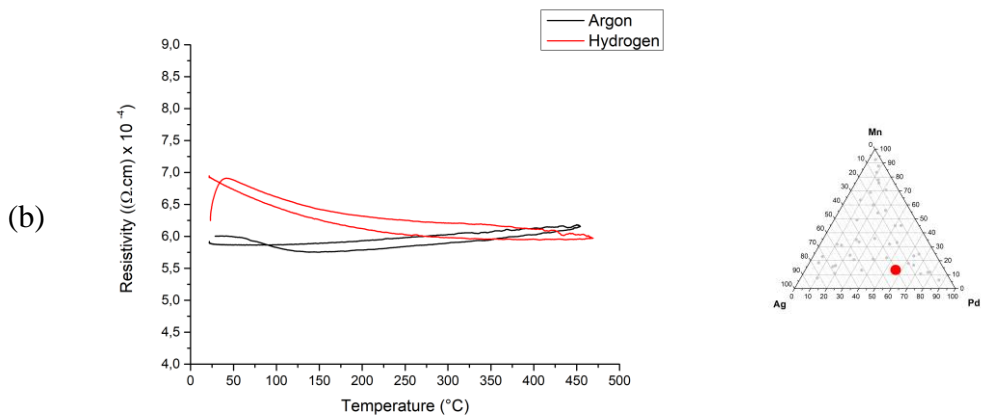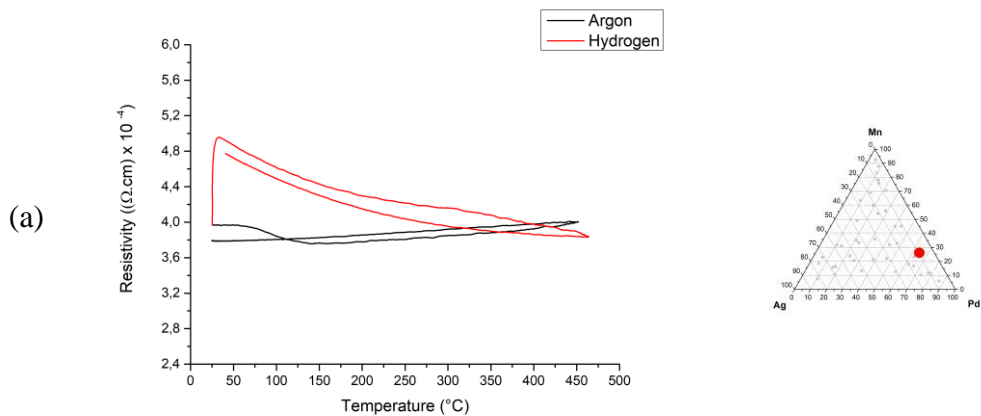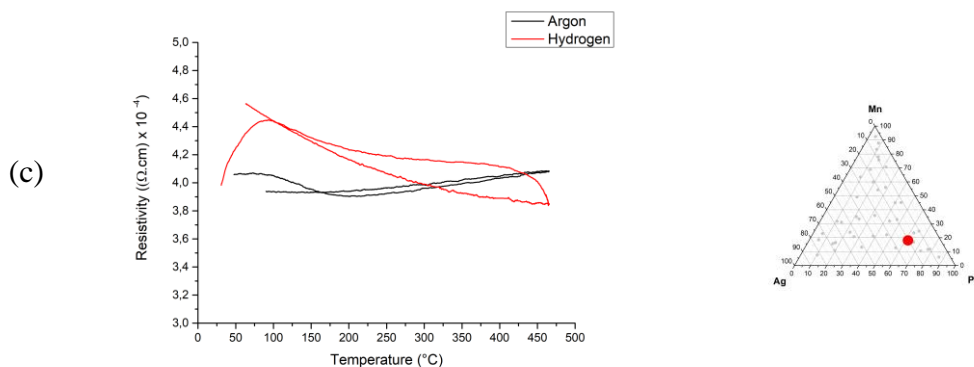
Figure 5.15. Resistivity measurement plots of compositions of which reacts with hydrogen (a) $Pd_{65}Mn_{25}Ag_{10}$, (b) $Pd_{57}Mn_{13}Ag_{30}$, (c) $Pd_{62}Mn_{18}Ag_{20}$, (d) $Pd_{46}Mn_{22}Ag_{32}$ and their positions in the ternary diagram.

The samples reported above are close to the Pd-Ag line towards the silver side. In the case of samples on the Pd side, the behavior was quite different. As seen in Figure 5.15, the resistivity curves with hydrogen differ quite significantly from those under argon. As soon as the samples were exposed to hydrogen, there was a sudden rise in resistivity. Upon heating, there is a decrease in resistivity, implying that the solubility of hydrogen decreases with an increase in temperature. The resistivity reaches the same value as those under argon at temperatures that range from 400 °C to 450 °C, depending on the sample. Upon cooling, the resistivity rises and remains high at room temperature.

So as to describe the behavior of the membranes in detail, reactivity indices were calculated at different temperatures. As described in Chapter 3.3, the reactivity index refers to ρH2/ρAr, i.e., the ratio of resistivity under hydrogen to that under argon. The reactivity indices of the membranes where $\rho H_2/\rho Ar > 1$ are tabulated in Table 5.5. Here the values refer to the heating cycle both in argon and hydrogen.

Table 5.5. Pd-Mn-Ag ternary compositions and their reactivity indices for corresponding temperature

Compositions	$\rho H_2/\rho Ar$						
	Temperature						
	50ºC	**100 ºC**	**150 ºC**	**200 ºC**	**250 ºC**	**350 ºC**	**400 ºC**
$Pd_{44}Mn_{45}Ag_{11}$	1.044	1.087	1.111	1.118	1.110	1.065	1.032
$Pd_{65}Mn_{25}Ag_{10}$	1.230	1.208	1.176	1.138	1.108	1.051	1.014
$Pd_{46}Mn_{22}Ag_{32}$	1.163	1.128	1.101	1.083	1.064	1.022	1.005
$Pd_{35}Mn_{13}Ag_{52}$	1.078	1.075	1.061	1.056	1.034	1.005	1.000
$Pd_{56}Mn_{13}Ag_{31}$	1.145	1.136	1.119	1.095	1.080	1.047	1.017
$Pd_{43}Mn_{32}Ag_{25}$	1.014	1.061	1.065	1.051	1.032	1.020	1.014
$Pd_{63}Mn_{23}Ag_{14}$	1.563	1.521	1.364	1.173	1.139	1.121	1.083
$Pd_{23}Mn_{24}Ag_{53}$	1.028	1.039	1.027	1.013	1.015	1.007	1.008
$Pd_{38}Mn_{21}Ag_{41}$	1.122	1.126	1.096	1.073	1.054	1.030	1.018
$Pd_{62}Mn_{18}Ag_{20}$	1.024	1.110	1.092	1.091	1.069	1.055	1.035
$Pd_{77}Mn_{12}Ag_{11}$	1.318	1.243	1.160	1.123	1.032	1.061	1.055

Reactivity indices are shown plotted in Figure 5.16 as contour maps. The maps refer to indices as determined at temperatures 50, 100, 150, 200, 250, 300, 350, and 400 ºC. The position of the samples for which the mapping is carried out is shown in Figure 5.16. Regions in white cover samples could not be evaluated due to their brittleness or the lack of compositions.

(a)　　　　　　　　　　　　　　　　　(b)
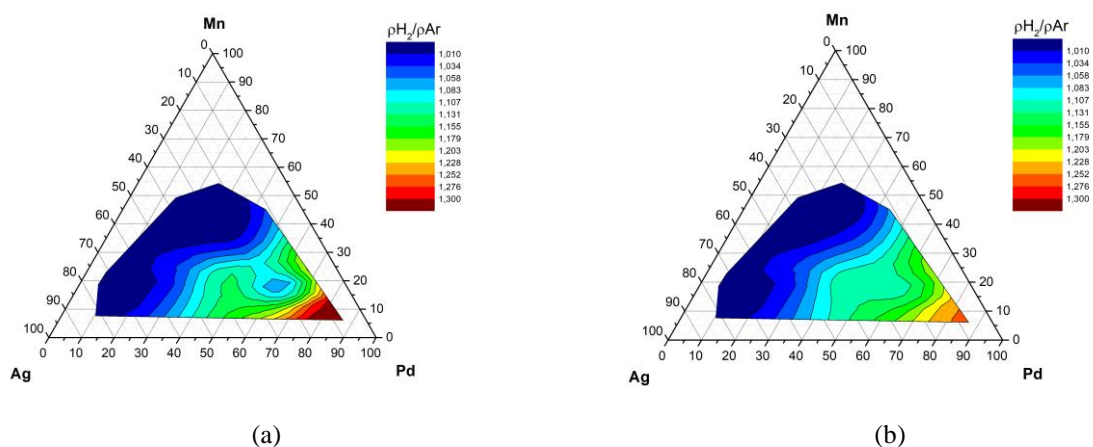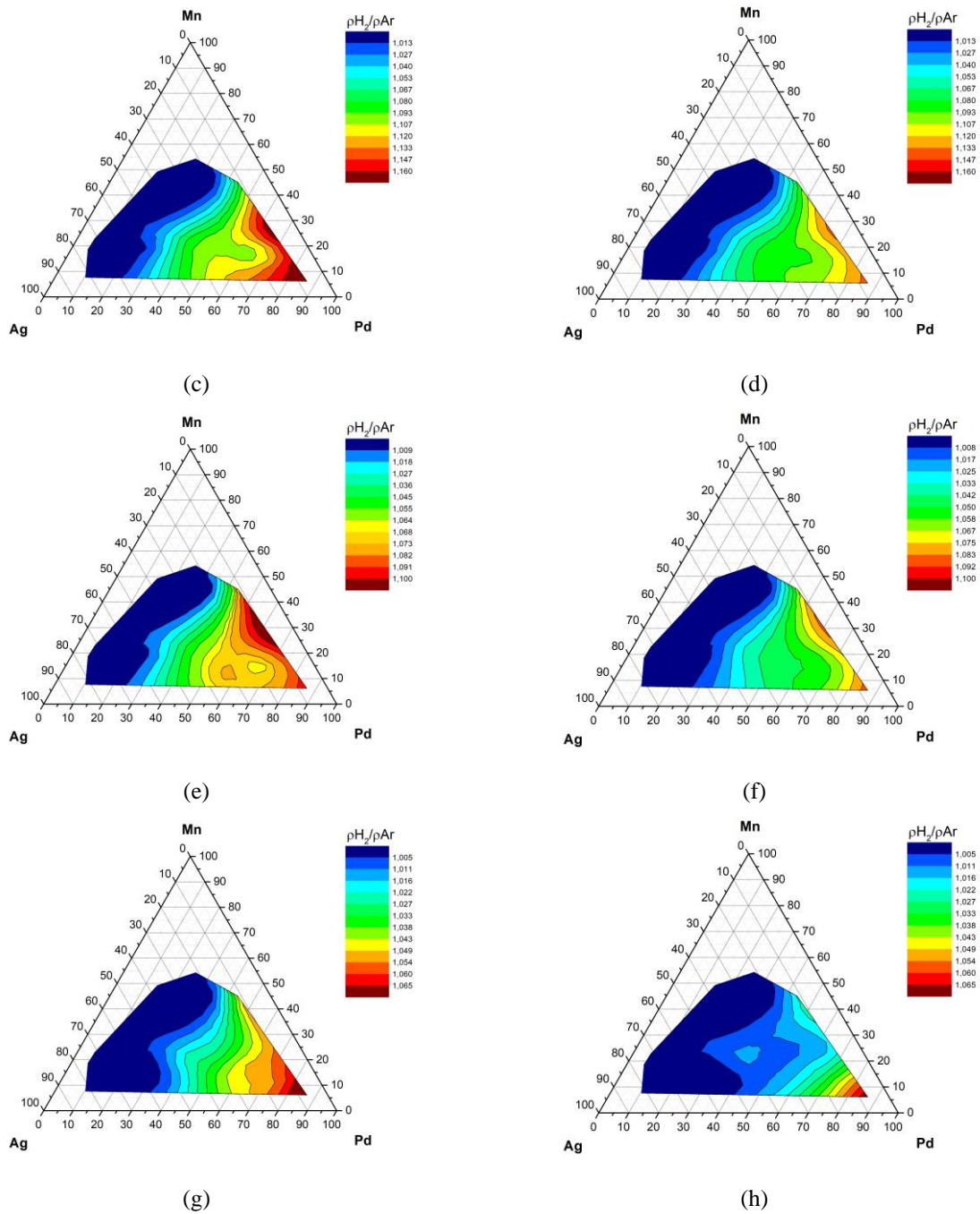
Figure 5.16. Contour Mapping of reactivity index in Pd-Mn-Ag ternary system. The positions of samples are shown in a). The map refers to temperatures of (a) 50 $^{\circ}$C, (b) 100 $^{\circ}$C, (c) 150 $^{\circ}$C, (d) 200 $^{\circ}$C (e) 250 $^{\circ}$C (f) 300 $^{\circ}$C (g) 350 $^{\circ}$C (h) 400 $^{\circ}$C.

Figure 5.16 gives these maps starting from 50°C to 400°C with 50°C intervals. As can be seen from the maps, the index values change with temperature. The

64

temperatures at which the reactivity indices reach their maximum were determined and tabulated in descending order in Table 5.6.

Table 5.6. Compositions and corresponding reactivity indices for their potential operation temperatures.

Pd (at.%)	Mn (at.%)	Ag (at.%)	$\rho H_2/\rho Ar$	Temperature
<u>56</u>	<u>13</u>	<u>31</u>	<u>1.047</u>	<u>350 °C</u>
44	45	11	1.118	200 °C
43	32	25	1.053	150 °C
23	24	53	1.030	100 °C
<u>62</u>	<u>18</u>	<u>20</u>	<u>1.096</u>	100 °C
65	25	10	1.226	50 °C
46	22	32	1.163	50 °C
38	21	41	1.122	50 °C
<u>35</u>	<u>13</u>	<u>52</u>	<u>1.078</u>	<u>50 °C</u>
63	23	14	1.563	<u>50 °C</u>
77	12	11	1.318	50 °C

(_) underlined compositions are the ones that are selected as candidate compositions.

(a)   (b)
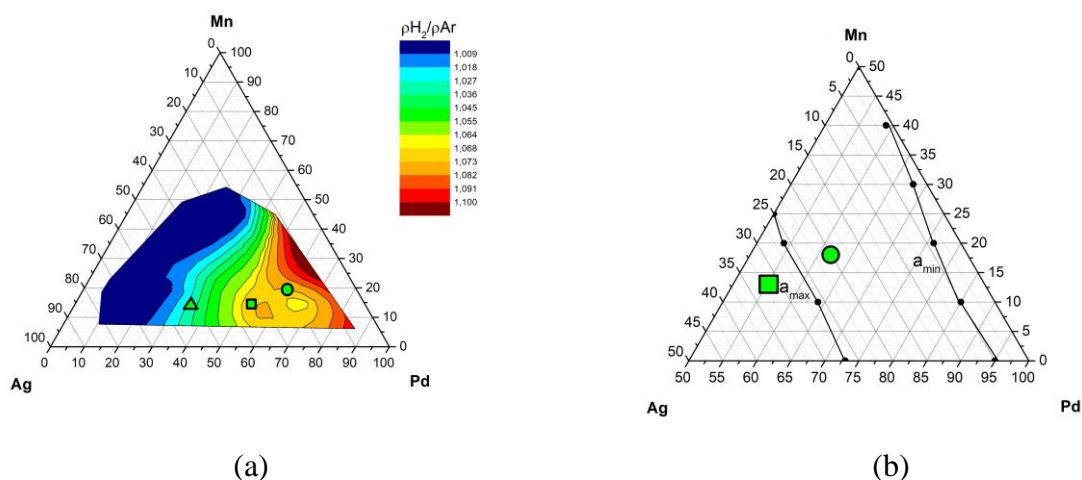
Figure 5.17. (a) Ternary contour mapping based on compositions' reactivity indices at 250 °C, also the positions of candidate compositions are given; green triangle legend represents $Pd_{35}Mn_{13}Ag_{52}$, green square legend represents $Pd_{56}Mn_{13}Ag_{31}$, and green circle legend represents $Pd_{62}Mn_{18}Ag_{20}$ (b) lattice parameter boundaries of $a_{min}=$ 3.905 Å and $a_{max} = 3.945$ Å calculated based on Vegard's law.

It may be pointed out that the reactivity index measures hydrogen solubility. Therefore, a higher index value should be preferred as it implies higher solubility. It

may be emphasized that permeability is the product of solubility with diffusivity. Therefore, the selection of membrane should be made by taking this into account. For this reason, we have selected the map for 250 °C. This map is shown redrawn in Figure 5.17(a).

A further consideration in f.c.c. hydrogen separation membranes refer to the lattice parameter of the membrane. Table 5.7 lists f.c.c. membranes and their lattice parameters, as well as their permeabilities. As seen in the table given, alloys have lattice constants varying between 3.905 Å to 3.945 Å. Thus, it would be useful to mark regions in the current map where the lattice parameters are in the same range as $3.905 < a < 3.945$ Å.

Atomic radii of Pd and Ag have values of 1.375 Å and 1.446 Å in coordination number of 12. These are calculated from the lattice parameter of the Pd and the Ag, which have values of 3.889 Å and 4.091 Å. The value of the atomic radius of the Mn could not found for the same coordination number. This value was derived from Table 5.4 by minimizing the error between the calculated and measured lattice parameters. This has yielded a value of 1.3731 Å. Using the atomic radii of Pd, Ag and Mn, the boundaries, where $a_{min}=3.905$ Å and $a_{max}=3.945$ Å, are marked in Figure 5.17(b).

Table 5.7. Some f.c.c. structured hydrogen separation membranes with their lattice parameters and permeability values.

Alloy composition (at.%)	Lattice Constant (Å)	Permeability at 350 °C ($\times 10^{-8}$ mol/m.s.Pa$^{1/2)}$	References
$Pd_{77}Ag_{23}$	3.931	3.21	[39] [83]
$Pd_{95}Au_5$	3.905	1.49	[84] [85]
$Pd_{92}Y_8$	3.945	3.92	[59] [85]

Three compositions are selected for further study. These are indicated in Figure 5.17 (a) and (b). They refer to compositions $Pd_{35}Mn_{13}Ag_{52}$, $Pd_{56}Mn_{13}Ag_{31}$, and $Pd_{62}Mn_{18}Ag_{20}$. The choice was made based on Pd content as well as the reactivity index. At the selected temperature of 250°C, the selected compositions have

reactivity indices of 1.034, 1.080, and 1.069. It should be noted that, of the three, only the last composition falls in between the boundaries drawn based on lattice parameters.

Of the three compositions, $Pd_{56}Mn_{13}Ag_{31}$ and $Pd_{62}Mn_{18}Ag_{20}$ are likely to show a higher permeability, but they are quite rich in their Pd content. The remaining $Pd_{35}Mn_{13}Ag_{52}$ have much less Pd, where its content is almost half of the commercial $Pd_{77}Ag_{23}$.

5.3   Permeability Measurements for Candidate Compositions

This section covers preparation of the nanoporous support material for thin film membranes as well as permeability measurements carried out for selected membranes.

5.3.1   Preparation of Nanoporous Support Substrate via Vacuum Thermal Dealloying

The set-up used for thermal dealloying was described in detail in Chapter 3.5. The starting material was Cu-Zn30at.% single phase α-brass in the form of foil 25 μm thick. Temperature and duration of dealloying are listed in table Table 5.8.

Table 5.8. Thermal dealloying treatments used for α-brass

Temperature (ºC)	Time (hour)
430	6
450	4
450	6
450	8
460	4
460	6
470	2
470	4
480	2
480	4
480	6
510	4

a)   b)

Figure 5.18. α-brass (a) before and (b) after the thermal dealloying. Note that the diameter remains the same.
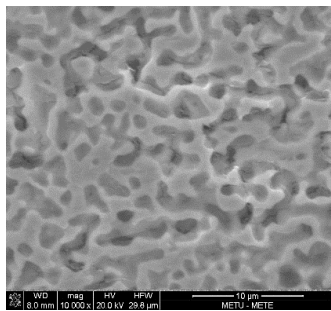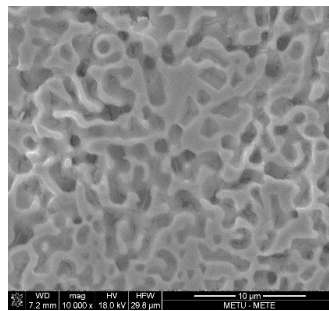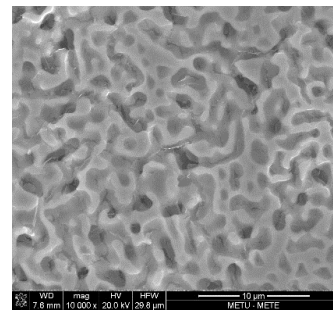
(a)   (b)   (c)
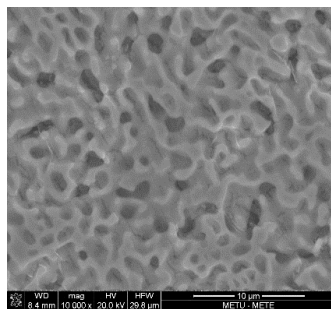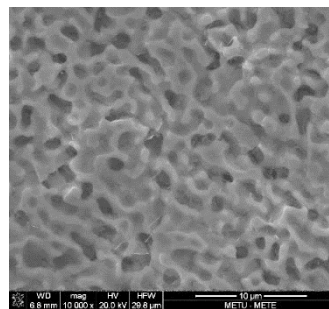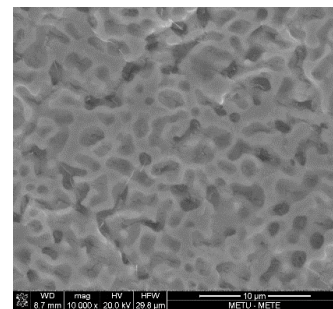
(d)   (e)   (f)
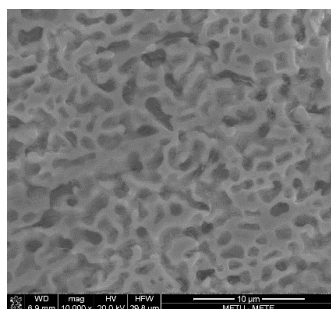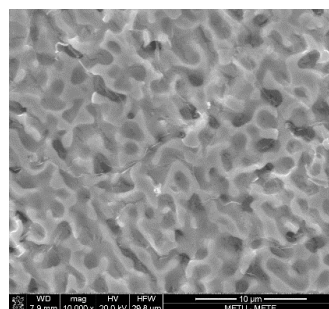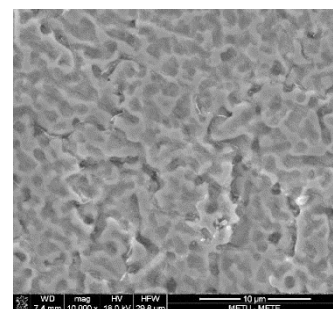
(g)   (h)   (i)

Figure 5.19. Surface images of brasses which are dealloyed at (a) 430 ºC-6 hours (b) 450 ºC-4 hours, (c) 450 ºC-8 hours, (d)460 ºC-4 hours (e) 460 ºC-6 hours, (f) 480 ºC-2 hours (g)480 ºC-4 hours (h) 480 ºC-6 hours and (i) 510 ºC- 4 hours.

Figure 5.19 shows representative SEM images taken from the dealloyed brass. he structures are similar, each displaying pores of approximately 1 mm in size. The dealloyed brass discs were tested for their permeability using the permeability tester described in section 3.4. For this purpose, dealloyed discs were loaded onto the set-up and tested with compressed air. The pressure was changed from 1 up to 4 bar. The pressure from the exit side was measured together with the flow rate. The results are plotted in the form of flow rate versus the pressure difference.
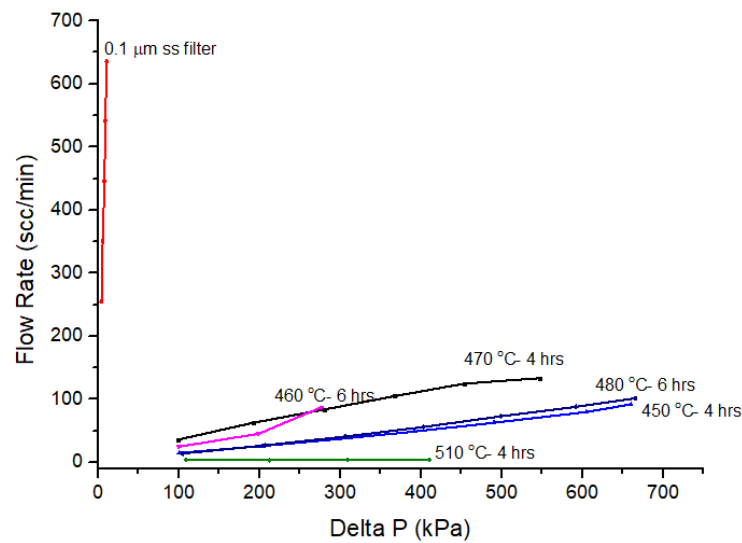
Figure 5.20. Pressure difference versus flow rate plot for dealloyed brasses under different conditions

Figure 5.20 shows the permeability of the dealloyed brass. Also included in the test was 0.1 µm grade stainless steel filter (Mott). It is seen that the permeability of the current dealloyed brass is significantly less than that of 0.1 µm grade stainless steel filter. It should be noted that there is no flow in the brass dealloyed at 430 ºC for 6 hours. This implies that pores generated on the discs' surface do not penetrate across the discs' thicknesses. The other discs dealloyed at 460 ºC up to 480 ºC are permeable. At 500 ºC however, there is no permeability of air through the substrates. This was due to sintering of the pores. An example of SEM micrograph showing the closure of pores at elevated temperature is given in Figure 5.21(a).

69
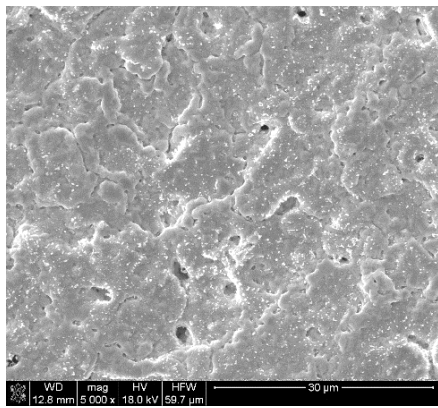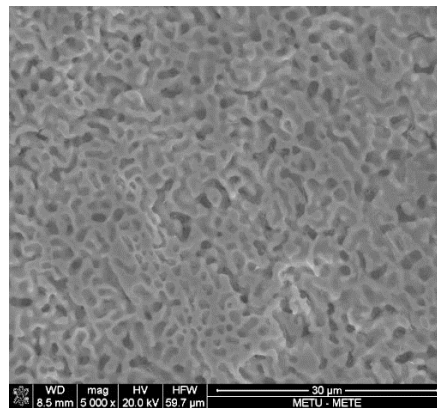
| (a) | (b) |

Figure 5.21. SEM micrograph of α-brass foil dealloyed at a) 600 ºC for 4 hours, b) at 460 for 4 hours. Note that at 600 ºC, dealloyed brass sintered together leaving behind a few pores.

As seen in Figure 5.20, brass dealloyed at 460 ºC exhibited relatively better flow rates e.g., 100 scc/min under nearly 300 kPa pressure difference. It is seen that the temperatures above 470 ºC, the flow rates are decreased gradually. This was also true for temperatures less than 460 ºC. Thus, as a result of these observations, a brass was dealloyed at 460 ºC for 4 hours.

5.3.2 Deposition of Pd-Mn-Ag Membranes onto Porous Substrates

Prior to sputter deposition of selected membranes onto porous dealloyed substrates, an initial experiment was carried out using glass substrates to recheck the compositions. Since the sputter deposition unit was redesigned, different power settings were necessary so as to obtain similar membranes in terms of compositions, given in Table 5.9. Chemical analyses of the coating are given in Table 5.10.

Table 5.9. Sputtering parameters used in membrane deposition

Target Metal	Gun	Power Applied (W)	Rate (Å/sec)
Ag	RF	15	1.3-1.4
Mn	RF	70	1.3-1.4
Pd	RF	25	1.3-1.4

The membrane compositions selected for further study was $Pd_{35}Mn_{13}Ag_{52}$, $Pd_{56}Mn_{13}Ag_{31}$ and $Pd_{62}Mn_{18}Ag_{20}$. Since there were some differences in the chemical compositions listed in Table 5.9, we have selected samples with position numbers 14, 15, and 18, which have compositions $Pd_{58}Mn_{15}Ag_{27}$, $Pd_{67}Mn_{14}Ag_{19}$, and $Pd_{34}Mn_9Ag_{57}$, respectively. The positions of the selected membranes were marked in Table 5.10.
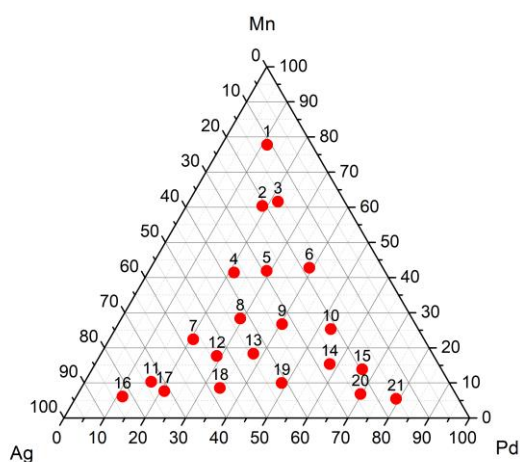
Figure 5.22. Composition distribution of the membranes to be deposited on dealloyed brass.
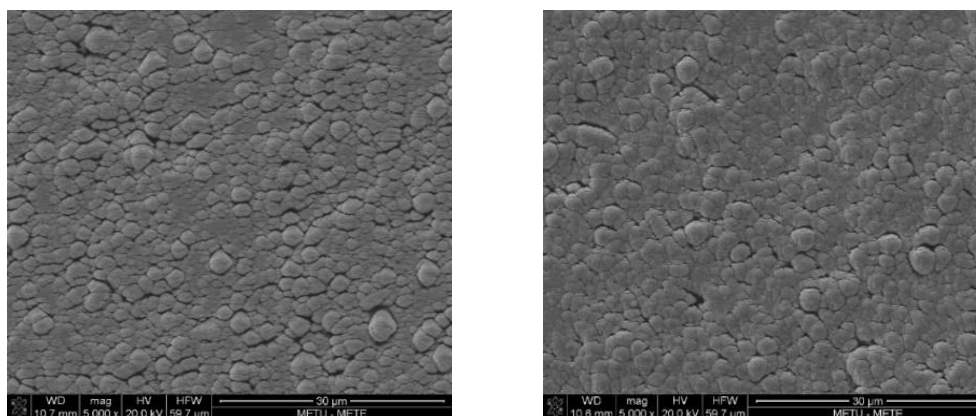
(a)   (b)

Figure 5.23. Representative surface morphologies obtained by SEM for the compositions of (a) $Pd_{38}Mn_{18}Ag_{44}$ and (b) $Pd_{58}Mn_{15}Ag_{27}$.

Table 5.10. Compositions of the membranes deposited for permeability measurements

Sample No	Pd (at.%)	Mn (at.%)	Ag (at.%)
1	11	78	11
2	19	60	21
3	22	62	16
4	21	42	37
5	29	42	29
6	39	43	18
7	21	22	57
8	29	28	43
9	40	27	33
10	53	25	22
11	17	10	73
12	29	18	53
13	38	18	44
14*	58	15	27
15*	67	14	19
16	11	6	83
17	21	8	71
18*	34	9	57
19	49	10	41
20	70	7	23
21	79	6	15

(*) represents membranes deposited on nanoporous dealloyed brass.
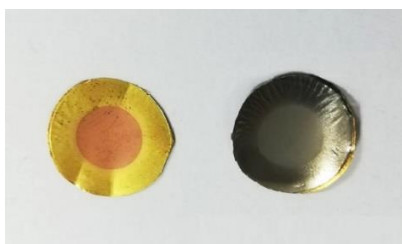
Figure 5.24. Photograph of dealloyed brass, before and after deposition.

The deposition time was set to be 11 hours so as to obtain 5 µm thick membranes. A photograph of membrane deposited on dealloyed brass is given in Figure 5.24. The inner 10 mm portion of the substrate can still be identified with its different morphology.

5.3.3   Permeability Measurement

Deposited membranes were then tested for their permeability. First, a check was made using argon for leak tightness. Unfortunately, the membrane leaked with 40 scc/min; therefore, testing was discontinued.
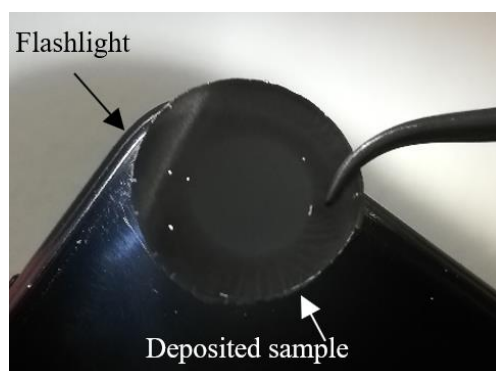
Figure 5.25. Image of the membrane deposited onto dealloyed brass illuminated by flashlight at the back. Bright spots on the membrane shows holes in the assembly.

Figure 5.25 shows one of the membranes which showed leakage during the testing. The image shows the photograph of the membrane in flashlight. White spots are visible, showing where there was leakage in the membrane. The leakage mainly occurred at the periphery of the dealloyed region, i.e., boundary between 10 mm dealloyed region and the brass periphery. Therefore, nanoporous dealloyed brass was not strong enough to withstand pressure applied onto it.

The membranes were also checked for their structure. SEM micrograph taken from the surface of the membrane are given in the Figure 5.23. It is seen that the deposits have typical cauliflower structure. Small voids are seen in the microstructure of each film. The leakage was attributed to the presence of these voids.

It is concluded that preparation of porous substrates using dealloying is quite favorable in yielding small size pores, but this, at the same time, weakens the substrate so that it cannot sustain its structural integrity during the measurement.

Candidate thin film alloys were also fabricated using proprietary nanoporous substrates. This time so as to avoid cauliflower structure[86] which was obtained in

the precious deposition and not fully dense, deposition was carried out with substrate heating. Also, deposition was carried out at a lower pressure. Thus, the substrates were heated to 350 °C, and the deposition was carried out at 4 mbar instead of the usual 7 mbar. The power settings were adjusted so that the deposition rate was reduced to half, i.e., 0.6 Å/s for each gun, and the settings were adjusted to keep the deposition rate the same during the 30-hour deposition

Thin film membranes on the proprietary nanoporous substrates with compositions $Pd_{35}Mn_{12}Ag_{53}$, $Pd_{37}Mn_{22}Ag_{41}$, $Pd_{57}Mn_{13}Ag_{30}$, and $Pd_{61}Mn_{18}Ag_{21}$ were fabricated. SEM images of the deposited membranes are given in Figure 5.26.

(a)

(b)

(c)

(d)
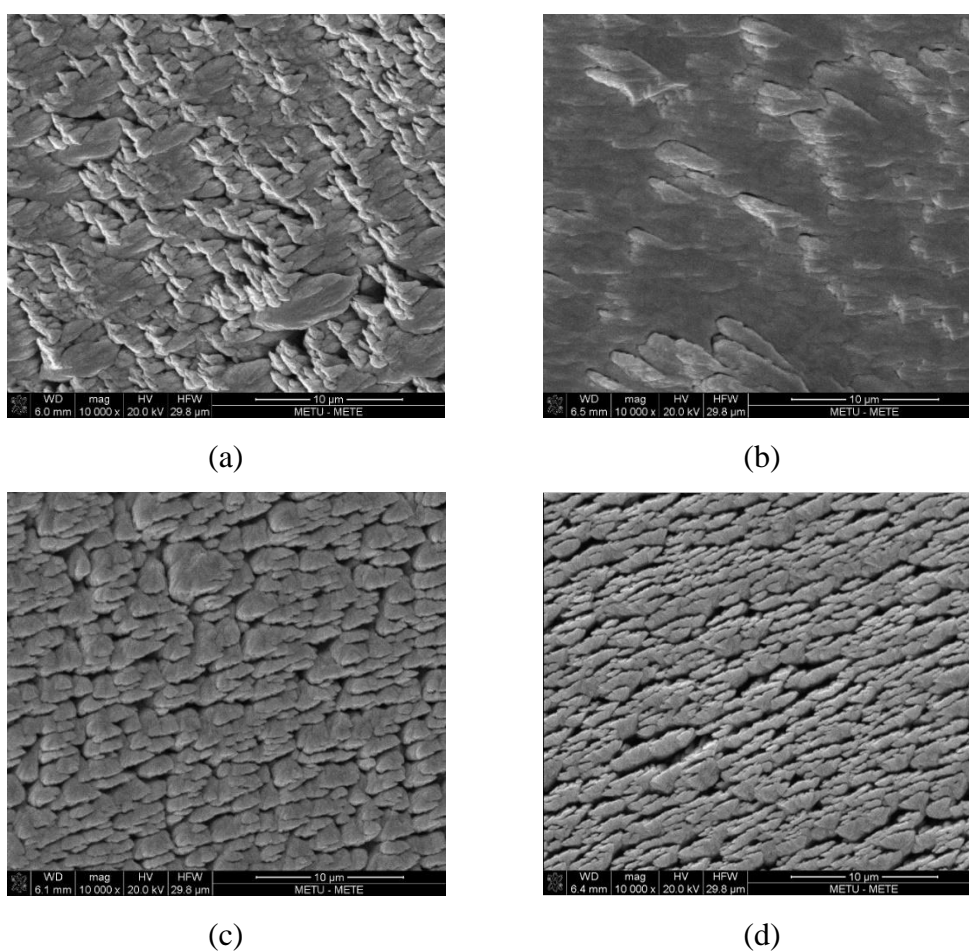
Figure 5.26. SEM images of thin film membranes which are deposited onto proprietary substrates with compositions of (a) $Pd_{37}Mn_{22}Ag_{41}$, (b) $Pd_{35}Mn_{12}Ag_{53}$, (c)$Pd_{57}Mn_{13}Ag_{30}$, and (d) $Pd_{61}Mn_{18}Ag_{21}$.

The structures, as seen in Figure 5.26, have improved somewhat as a result of changes in the deposition conditions. In Figure 5.26 (b) the structure appears to be fully dense, i.e., $Pd_{35}Mn_{12}Ag_{53}$, the structures in other membranes are not too far off from the cauliflower structure.

The films are subjected to permeability measurements and tested for gas tightness under argon flow. The membranes $Pd_{61}Mn_{18}Ag_{21}$, when tested with argon, leaked with a flow rate in excess of 15 scc/min (at 4 bar inlet pressure). The membranes $Pd_{35}Mn_{12}Ag_{53}$, $Pd_{37}Mn_{22}Ag_{41}$, $Pd_{57}Mn_{13}Ag_{30}$ also leaked, but the flow rate was quite low, i.e., 2 scc/min at 4 bar inlet pressure of argon.

The membranes $Pd_{35}Mn_{12}Ag_{53}$, $Pd_{37}Mn_{22}Ag_{41}$, $Pd_{57}Mn_{13}Ag_{30}$, since they have a relatively small leak were subjected to permeability measurements since the permeability can still be determined despite leakage.

An example of data collected during the measurement is given in Table 5.11 for $Pd_{35}Mn_{12}Ag_{53}$. Here, first, the membrane was tested at 300 ^{o}C. This has given an argon flow rate of 2.5 scc/min (at 4 bar inlet pressure). The flow rate in the case of hydrogen was initially 16 scc/min. This value is the same as argon when corrected for its diffusivity. The flow rates of gases are inversely proportional to square root of their molecular weight[87]. That is, hydrogen flow through porous media is expected to be 6.3 times that of argon. The measured flow rate of hydrogen is 8.66 times that of argon which is quite close to the expected value of 6.3.

Table 5.11 Pressure differences and corresponding flow rates of argon and hydrogen for the membrane $Pd_{35}Mn_{12}Ag_{53}$ at 300 ^{o}C.

ΔP_{Ar} (kPa)	Flow rate (Ar) (scc/min)	ΔP_{H2} (kPa)	Flow rate (H_2) (scc/min)
71	0.50	61	3.90
127	0.90	129	8.50
178	1.35	168	11.10
217	1.60	223	15.60
287	2.30	264	18.65
313	2.50	301	21.65

The initial flow rate of hydrogen, which was 16 scc/min (at $\Delta P= 301$ kPa) increased with time. After 30 minutes the flow rate has reached a steady state at 21.65 scc/min. The membrane was tested with argon again. This has yielded a flow rate of 3.15 scc/min, which was higher than the initial value. The actual measured rate after 30 minutes, when converted into that of argon using a factor of 6.3, was 19.86 scc/min, which was very close to the measured flow rate. This indicates that the membrane assembly was somehow damaged during testing. The case with other membranes was also similar.

CHAPTER 6

GENERAL CONCLUSION

A study was carried out into dense metallic membranes for hydrogen separation. Two palladium-based systems were characterized for Pd-Co-Ni and Pd-Mn-Ag. Membranes were produced via sputter deposition in combinatorial geometry. For this purpose, sputter targets were arranged in triangular manner, and there were a total of 21 substrates just above the targets. Membranes were screened via resistivity measurements under argon and hydrogen carried out up to 450 $^{\circ}$C. A reactivity index defined as resistivity under hydrogen over that in argon was used as an index of the suitability of the thin film membranes for hydrogen separation. The following conclusions can be drawn from this study;

1- In the Pd-Co-Ni system, except for the small region close to the Co corner, the rest of the ternary field had f.c.c structure. Unfortunately, these membranes under the current measurement conditions (1 bar hydrogen up to 450 $^{\circ}$C) showed no reaction with hydrogen, and therefore they were unsuitable as separation membranes.

2- Pd-Mn-Ag also had a wide compositional field with f.c.c. structure. These were close to the Ag-Pd line. Moreover, a considerable fraction of these membranes reacted with hydrogen implying that they may be suitable as separation membranes.

3- Based on their performances and Pd content, three membrane compositions, namely $Pd_{35}Mn_{13}Ag_{52}$, $Pd_{56}Mn_{13}Ag_{31}$, and $Pd_{62}Mn_{18}Ag_{20}$ were selected as candidates for hydrogen separation.

Selected compositions were then sputter deposited on dealloyed brass as support material for permeability measurements. Dealloying was carried out at 460 °C for 4 hours under vacuum (10^{-6} mbar). This has yielded copper substrate with pores of approximately 1 μm in size. Thin film membranes of 5 μm thick were deposited on the nanoporous copper. Unfortunately, measurements were not possible as the coated assemblies were not gas tight. A thicker deposition 7 μm thick with substrate heating to 350 °C on a proprietary substrate also failed as these assemblies were not structurally stable during testing.

Further work would be needed to improve i) nanoporous substrate so that it is sufficiently fine and structurally sound so that it can support the sputter deposited separation membrane. ii) Deposited membranes should be improved further, i.e., in addition to reduced pressure during sputtering and substrate heating, the rotation of the substrate would be useful so as to improve the density of the deposited film further.

It is further recommended that before the actual membrane was manufactured, either as thin film coated on the nanoporous membrane or in the form of foil or tubes, the selected compositions may be subjected to further tests. These tests may involve resistivity measurement with a number of cycles, so that the resistivity curve is stabilized. Also, it is recommended that the test is repeated at different pressure levels so that the performance of the membrane is known under different conditions.

REFERENCES

[1] Hydrogen production: Natural gas reforming. EnergyGov n.d. https://www.energy.gov/eere/fuelcells/hydrogen-production-natural-gas-reforming (accessed January 11, 2022).

[2] Sircar S, Golden TC. Pressure Swing Adsorption Technology for Hydrogen Production. Hydrog. Syngas Prod. Purifi cation Technol., 2010, p. 414–50.

[3] Al-Mufachi NA, Rees N V., Steinberger-Wilkens R. Hydrogen selective membranes: A review of palladium-based dense metal membranes. Renew Sustain Energy Rev 2015;47:540–51. https://doi.org/10.1016/j.rser.2015.03.026.

[4] Ockwig NW, Nenoff TM. Membranes for hydrogen separation. Chem Rev 2007;107:4078–110. https://doi.org/10.1021/cr0501792.

[5] Dolan MD, Dave NC, Ilyushechkin AY, Morpeth LD, McLennan KG. Composition and operation of hydrogen-selective amorphous alloy membranes. J Memb Sci 2006;285:30–55. https://doi.org/10.1016/j.memsci.2006.09.014.

[6] Dolan MD. Non-Pd BCC alloy membranes for industrial hydrogen separation. J Memb Sci 2010;362:12–28. https://doi.org/10.1016/j.memsci.2010.06.068.

[7] Spath PL, Dayton DC. Preliminary Screening -- Technical and Economic Assessment of Synthesis Gas to Fuels and Chemicals with Emphasis on the Potential for Biomass-Derived Syngas. Natl Renew Energy Lab 2003:1–160. https://doi.org/10.2172/15006100.

[8] Lang Y, Arnepalli RR, Tiwari A. A review on hydrogen production: Methods, materials and nanotechnology. J Nanosci Nanotechnol 2011;11:3719–39. https://doi.org/10.1166/jnn.2011.4157.

[9] Neubauer Y, Liu H. Biomass gasification. Biomass Combust Sci Technol Eng 2013;8:106–29. https://doi.org/10.1533/9780857097439.2.106.

[10] GRHYD Inauguration. McPhy 2018. https://www.engie.com/

en/journalists/press-releases/grhyd-inaugurate-frances-first-power-to-gas-demonstrator/(accessed January 11, 2022).

[11]   Isaac T. HyDeploy : The UK ' s First Hydrogen Blending Deployment Project 2019;3:114–25. https://doi.org/10.1093/ce/zkz006.

[12]   Maqsood K, Mullick A, Ali A, Kargupta K, Ganguly S. Cryogenic carbon dioxide separation from natural gas: A review based on conventional and novel emerging technologies. Rev Chem Eng 2014;30:453–77. https://doi.org/10.1515/revce-2014-0009.

[13]   Baldwin M, Ghavami A, Ghiaasiaan SM, Majumdar A. Flow boiling in liquid hydrogen, liquid methane and liquid oxygen: A review of available data and predictive tools. Cryogenics (Guildf) 2021;116:103298. https://doi.org/10.1016/j.cryogenics.2021.103298.

[14]   Miller GQ, Stoecker J. Selection of a hydrogen separation process 1989.

[15]   Rackley SA. Membrane Separation Systems. 2013. https://doi.org/10.1016/b978-1-85617-636-1.00008-0.

[16]   Yukawa H, Nambu T, Matsumoto Y. Design of group 5 metal-based alloy membranes with high hydrogen permeability and strong resistance to hydrogen embrittlement. Woodhead Publishing Limited; 2014. https://doi.org/10.1533/9780857097736.3.341.

[17]   Lai T, Yin H, Lind ML. The hydrogen permeability of Cu-Zr binary amorphous metallic membranes and the importance of thermal stability. J Memb Sci 2015;489:264–9. https://doi.org/10.1016/j.memsci.2015.03.098.

[18]   Itoh N, Xu WC, Hara S, Kimura HM, Masumoto T. Permeability of hydrogen in amorphous $Pd((1-\chi))Si(\chi)$ alloys at elevated temperatures. J Memb Sci 1998;139:29–35. https://doi.org/10.1016/S0376-7388(97)00238-X.

[19]   Hara S, Hatakeyama N, Itoh N, Kimura HM, Inoue A. Hydrogen permeation through palladium-coated amorphous Zr-M-Ni (M = Ti, Hf) alloy membranes. Desalination 2002;144:115–20. https://doi.org/10.1016/S0011-

9164(02)00298-9.

[20]   Hara S, Sakaki K, Itoh N, Kimura HM, Asami K, Inoue A. An amorphous alloy membrane without noble metals for gaseous hydrogen separation. J Memb Sci 2000;164:289–94. https://doi.org/10.1016/S0376-7388(99)00192-1.

[21]   Yamaura SI, Shimpo Y, Okouchi H, Nishida M, Kajita O, Inoue A. The Effect of Additional Elements on Hydrogen Permeation properties of Melt-Spun Ni-Nb-Zr Amorphous Alloys. Mater Trans 2004;45:330–3. https://doi.org/10.2320/matertrans.45.330.

[22]   Fukai Y. The Metal-Hydrogen System. 1st ed. Berlin, Heidelberg: Springer; 1993.

[23]   Paglieri SN, Wermer JR, Buxbaum RE, Ciocco M V., Howard BH, Morreale BD. Development of membranes for hydrogen separation: Pd coated V-10Pd. Energy Mater Mater Sci Eng Energy Syst 2008;3:169–76. https://doi.org/10.1179/174892409X427931.

[24]   Siriwardane R V., Poston JA, Fisher EP, Lee TH, Dorris SE, Balachandran U. Characterization of ceramic hydrogen separation membranes with varying nickel concentrations. Appl Surf Sci 2000;167:34–50. https://doi.org/10.1016/S0169-4332(00)00493-1.

[25]   Komiya K, Ito S, Yukawa H, Morinaga M, Nagata K, Nambu T, et al. Alloying Effects on the Hydriding Properties of Niobium Metal. Mater Trans 2003;44:1686–9. https://doi.org/10.2320/matertrans.44.1686.

[26]   Hashi K, Ishikawa K, Matsuda T, Aoki K. Microstructures and hydrogen permeability of Nb-Ti-Ni alloys with high resistance to hydrogen embrittlement. Mater Trans 2005;46:1026–31. https://doi.org/10.2320/matertrans.46.1026.

[27]   Dolan MD, Viano DM, Langley MJ, Lamb KE. Tubular vanadium membranes for hydrogen purification. J Memb Sci 2018;549:306–11.

https://doi.org/10.1016/j.memsci.2017.12.031.

[28]   Edlund D, Friesen D, Johnson B, Pledger W. Hydrogen-permeable metal membranes for high-temperature gas separations. Gas Sep Purif 1994;8:131–6. https://doi.org/10.1016/0950-4214(94)80023-5.

[29]   Jewett D, Makrides AC, Wright MA. Separation of Hydrogen by Permeation, 1967.

[30]   Jo YS, Lee CH, Kong SY, Lee KY, Yoon CW, Nam SW, et al. Characterization of a Pd/Ta composite membrane and its application to a large scale high-purity hydrogen separation from mixed gas. Sep Purif Technol 2018;200:221–9. https://doi.org/10.1016/j.seppur.2017.12.019.

[31]   Cooney DA, Way JD, Wolden CA. A comparison of the performance and stability of Pd/BCC metal composite membranes for hydrogen purification. Int J Hydrogen Energy 2014;39:19009–17. https://doi.org/10.1016/j.ijhydene.2014.09.094.

[32]   Graham T. On the Absorbtion and Dialytic Separation of Gases by Colloid Septa. R Soc 1866;156:399–439.

[33]   Massalski T, Okamoto H, Subramanian P, Kacprzak L. Binary Alloy Phase Diagrams, 2nd Edition 1990.

[34]   Cheng YS, Yeung KL. Palladium-silver composite membranes by electroless plating technique. J Memb Sci 1999;158:127–41. https://doi.org/10.1016/S0376-7388(99)00009-5.

[35]   Flanagan TB, Wang D. Hydrogen permeation through fcc Pd-Au alloy membranes. J Phys Chem C 2011;115:11618–23. https://doi.org/10.1021/jp201988u.

[36]   Lewis AE, Kershner DC, Paglieri SN, Slepicka MJ, Way JD. Pd-Pt/YSZ composite membranes for hydrogen separation from synthetic water-gas shift streams. J Memb Sci 2013;437:257–64. https://doi.org/10.1016/j.memsci.2013.02.056.

[37] Doyle BML, Harris IR. Palladium-Rare Earth Alloys THEIR ORDER-DISORDER TRANSFORMATIONS AND BEHAVIOUR WITH HYDROGEN. Platin Met Rev, 1988;32:130–40.

[38] Gel'd P V., Shteinberg MM, Simakov YP, Gol'tsov VA. Diffusion and solubility of hydrogen in nickel-manganese alloys. Sov Mater Sci 1967;2:221–4. https://doi.org/10.1007/BF00714673.

[39] Fort D, Farr JPG, Harris IR. A comparison of palladium-silver and palladium-yttrium alloys as hydrogen separation membranes. J Less-Common Met 1974;39:293–308.

[40] Peters TA, Stange M, Bredesen R. On the high pressure performance of thin supported Pd-23%Ag membranes-Evidence of ultrahigh hydrogen flux after air treatment. J Memb Sci 2011;378:28–34. https://doi.org/10.1016/j.memsci.2010.11.022.

[41] Peters TA, Kaleta T, Stange M, Bredesen R. Hydrogen transport through a selection of thin Pd-alloy membranes: Membrane stability, H 2S inhibition, and flux recovery in hydrogen and simulated WGS mixtures. Catal Today 2012;193:8–19. https://doi.org/10.1016/j.cattod.2011.12.028.

[42] Zhang X, Xie X, Huang Y. Pure Ni and Pd-Ni alloy membranes prepared by electroless plating for hydrogen separation. Adv Mater Res 2011;179–180:1309–13. https://doi.org/10.4028/www.scientific.net/AMR.179-180.1309.

[43] Pişkin F, Akyildiz H, Öztürk T. Ti modified Pd-Ag membranes for hydrogen separation. Int J Hydrogen Energy 2015;40:7553–8. https://doi.org/10.1016/j.ijhydene.2014.11.049.

[44] Pişkin F, Öztürk T. Combinatorial screening of Pd-Ag-Ni membranes for hydrogen separation. J Memb Sci 2017;524:631–6. https://doi.org/10.1016/j.memsci.2016.11.066.

[45] Pişkin F, Öztürk T. Nb-Pd-Ti BCC thin films for hydrogen separation. J

Alloys Compd 2019;775:411–8. https://doi.org/10.1016/j.jallcom.2018.10.126.

[46] Mardilovich IP, Engwall E, Ma YH. Dependence of hydrogen flux on the pore size and plating surface topology of asymmetric Pd-porous stainless steel membranes. Desalination 2002;144:85–9. https://doi.org/10.1016/S0011-9164(02)00293-X.

[47] Lu Z, Li C, Han J, Zhang F, Liu P, Wang H, et al. Three-dimensional bicontinuous nanoporous materials by vapor phase dealloying. Nat Commun 2018;9:1–7. https://doi.org/10.1038/s41467-017-02167-y.

[48] Sun L, Chien CL, Searson PC. Fabrication of nanoporous nickel by electrochemical dealloying. Chem Mater 2004;16:3125–9. https://doi.org/10.1021/cm0497881.

[49] Hsueh HY, Huang YC, Ho RM, Lai CH, Makida T, Hasegawa H. Nanoporous gyroid nickel from block copolymer templates via electroless plating. Adv Mater 2011;23:3041–6. https://doi.org/10.1002/adma.201100883.

[50] Sacco L, Florea I, Cojocaru CS. Fabrication of porous anodic alumina (PAA) templates with straight pores and with hierarchical structures through exponential voltage decrease technique. Surf Coatings Technol 2019;364:248–55. https://doi.org/10.1016/j.surfcoat.2019.02.086.

[51] Kian K, Woodall C, Wilcox J, Liguori S. Performance of Pd-Based Membranes and Effects of Various Gas Mixtures on H2 Permeation. Environments 2018;5:128. https://doi.org/10.3390/environments5120128.

[52] Altinisik O, Dogan M, Dogu G. Preparation and characterization of palladium-plated porous glass for hydrogen enrichment. Catal Today 2005;105:641–6. https://doi.org/10.1016/j.cattod.2005.06.012.

[53] Yeung KL, Sebastian JM, Varma A. Novel preparation of Pd/Vycor composite membranes. Catal Today 1995;25:231–6. https://doi.org/10.1016/0920-5861(95)00077-S.

[54] Seo BS, Han JY, Lee KY, Kim DW, Ryi SK. Electroless Pd deposition on a planar porous stainless steel substrate using newly developed plating rig and agitating water bath. Korean J Chem Eng 2017;34:266–72. https://doi.org/10.1007/s11814-016-0256-6.

[55] Zahedi M, Afra B, Dehghani-Mobarake M, Bahmani M. Preparation of a Pd membrane on a WO3 modified Porous Stainless Steel for hydrogen separation. J Memb Sci 2009;333:45–9. https://doi.org/10.1016/j.memsci.2009.01.053.

[56] Ilias S, Su N, Udo-Aka UI, King FG. Application of electroless deposited thin-film palladium composite membrane in hydrogen separation. Sep Sci Technol 1997;32:487–504. https://doi.org/10.1080/01496399708003211.

[57] Jayaraman V, Lin YS, Pakala M, Lin RY. Fabrication of ultrathin metallic membranes on ceramic supports by sputter deposition. J Memb Sci 1995;99:89–100. https://doi.org/10.1016/0376-7388(94)00212-H.

[58] Jayaraman V, Lin YS. Synthesis and hydrogen permeation properties of ultrathin palladium-silver alloy membranes. J Memb Sci 1995;104:251–62. https://doi.org/10.1016/0376-7388(95)00040-J.

[59] Gobina E, Hughes R, Monaghan D, Arnell D. High-Temperature Selective Membranes for Hydrogen Separation. Dev Chem Eng Miner Process 1994;2:105–14. https://doi.org/10.1002/apj.5500020203.

[60] Honig RE. Vapor pressure data for the solid and liquid elements. RCA Laboratories, David SarnoffResearch Center; 1969.

[61] Yang C, Tian Y, Qu T, Yang B, Xu B. Analysis of the behavior of magnesium and CO vapor in the carbothermic reduction of magnesia in a vacuum. J Magnes Alloy 2014;2:50–8. https://doi.org/10.1016/j.jma.2014.02.003.

[62] Sun Y, Ren Y, Yang K. New preparation method of micron porous copper through physical vacuum dealloying of Cu-Zn alloys. Mater Lett 2016;165:1–4. https://doi.org/10.1016/j.matlet.2015.11.102.

[63]   Ren Y Bin, Sun YX, Yang K. Study on micron porous copper prepared by physical vacuum dealloying. Acta Metall Sin (English Lett 2016;29:1144–7. https://doi.org/10.1007/s40195-016-0505-z.

[64]   Han J, Li C, Lu Z, Wang H, Wang Z, Watanabe K, et al. Vapor phase dealloying: A versatile approach for fabricating 3D porous materials. Acta Mater 2019;163:161–72. https://doi.org/10.1016/j.actamat.2018.10.012.

[65]   Kosmidou M, Detisch MJ, Maxwell TL, Balk TJ. Vacuum thermal dealloying of magnesium-based alloys for fabrication of nanoporous refractory metals. MRS Commun 2019;9:144–9. https://doi.org/10.1557/mrc.2019.15.

[66]   Smits FM. Measurement of Sheet Resistivities with the Four-Point Probe. Bell Syst Tech J 1958;37:711–8. https://doi.org/10.1002/j.1538-7305.1958.tb03883.x.

[67]   Ishida K, Nishizawa T. The Co-Pd (Cobalt-Palladium) System. J Phase Equilibria 1991;12:83–7.

[68]   Nash A, Nash P. The Ni-Pd (Nickel-Palladium) System. vol. 5. 1984.

[69]   Nishizawa T, Ishida K. The Co-Ni (Cobalt-Nickel) system. Bull Alloy Phase Diagrams 1983;4:390–5. https://doi.org/10.1007/BF02868090.

[70]   Santucci A, Tosti S, Basile A. Alternatives to palladium in membranes for hydrogen separation: Nickel, niobium and vanadium alloys, ceramic supports for metal alloys and porous glass membranes. vol. 1. Woodhead Publishing Limited; 2013. https://doi.org/10.1533/9780857097330.1.183.

[71]   Muscat JP. Hydrogen heats of solution in Co, Ni, Cu, Rh, Pd and Ag. J Phys C Solid State Phys 1982;15:5551–7. https://doi.org/10.1088/0022-3719/15/27/012.

[72]   Stafford SW, McLellan RB. The solubility of hydrogen in nickel and cobalt. Acta Metall 1974;22:1463–8. https://doi.org/10.1016/0001-6160(74)90107-2.

[73]   Suzuki A, Yukawa H. nalysis for Reverse Temperature Dependence of

Hydrogen Permeability through Pd-X (X=Y, Ho, Ni) Alloy Membranes Based on Hydrogen Chemical Potential. Membranes (Basel) 2020;10.

[74] Okamoto H. Mn-Pd (Manganese-Palladium). vol. 14. 1993.

[75] I. Karakaya, W.T. Thompson. The Ag-Mn (Silver-Manganese) System. Bull Alloy Phase Diagrams 1990;11:480–6.

[76] Karakaya I, Thompson WT. The Ag-Pd (Silver-Palladium) System. Bull Alloy Phase Diagrams 1988;9:237–43.

[77] Lawson AC, Larson AC, Aronson MC, Johnson S, Fisk Z, Canfield PC, et al. Magnetic and crystallographic order in α-manganese. J Appl Phys 1994;76:7049–51. https://doi.org/10.1063/1.358024.

[78] Kjekshus A, Møllerud R, Andresen AF, Pearson WB. Equiatomic transition metal alloys of manganese. Philos Mag 1967;16:1063–83. https://doi.org/10.1080/14786436708229694.

[79] Pál L, Krén E, Kádár G, Szabó P, Tarnóczi T. Magnetic structures and phase transformations in Mn-Based CuAu-I type alloys. J Appl Phys 1968;39:538–44. https://doi.org/10.1063/1.2163510.

[80] Kádár G, Krén E. Crystal and magnetic structure of the Mn3Pd5 phase. Solid State Commun 1972;11:933–6.

[81] Baba K, Niki Y, Sakamoto Y, Flanagan TB. The phase transition in palladium-manganese alloys with up to 33.3 at.% Mn. J Alloys Compd 1992;179:321–31. https://doi.org/10.1016/0925-8388(92)90231-W.

[82] Holleck GL. Diffusion and solubility of hydrogen in palladium and palladium-silver alloys. J Phys Chem 1970;74:503–11. https://doi.org/10.1021/j100698a005.

[83] Pati S, Jat RA, Mukerjee SK, Parida SC. X-ray diffraction study of thermal parameters of Pd, Pd-Ag and Pd-Ag-Cu alloys as hydrogen purification membrane materials. Phys B Condens Matter 2016;484:42–7. https://doi.org/10.1016/j.physb.2015.12.048.

[84]   McKinley DL. Method for Hydrogen Separation and Purification, 1969. https://doi.org/10.2307/1190003.

[85]   Sakamoto Y, Chen FL, Ura M, Flanagan TB. Thermodynamic Properties for Solution of Hydrogen in Palladium-Based Binary Alloys. Ber Bunsenges Phys Chem 1995;99:807–20. https://doi.org/10.1016/0925-8388(95)02103-5.

[86]   Haghiri-Gosnet AM, Ladan FR, Mayeux C, Launois H, Joncour MC. Stress and microstructure in tungsten sputtered thin films. J Vac Sci Technol A Vacuum, Surfaces, Film 1989;7:2663–9. https://doi.org/10.1116/1.575770.

[87]   Ziarani AS, Aguilera R. Knudsen's Permeability Correction for Tight Porous Media. Transp Porous Media 2012;91:239–60. https://doi.org/10.1007/s11242-011-9842-6.